Large-Scale Uncertainty and Error Analysis for Time-dependent Fluid/Structure Interactions in Wind Turbine Applications

Award No.: DE-FG02-10ER26026; SC0005385

PI: Juan J. Alonso
Department of Aeronautics & Astronautics
Stanford University

Co-PI: Gianluca Iaccarino
Department of Mechanical Engineering
Stanford University

Report Date: August 25, 2013

Period Covered by Report: June 1, 2011 -May 31, 2013

1 Summary

The following is the final report covering the entire period of this aforementioned grant, June 1, 2011 - May 31, 2013 for the portion of the effort corresponding to Stanford University (SU). SU has partnered with Sandia National Laboratories (PI: Mike S. Eldred) and Purdue University (PI: Dongbin Xiu) to complete this research project and this final report includes those contributions made by the members of the team at Stanford. Dr. Eldred is continuing his contributions to this project under a no-cost extension and his contributions to the overall effort will be detailed at a later time (once his effort has concluded) on a separate project submitted by Sandia National Laboratories. At Stanford, the team is made up of Profs. Alonso, Iaccarino, and Duraisamy, post-doctoral researcher Vinod Lakshminarayan, and graduate student Santiago Padron. At Sandia National Laboratories, the team includes Michael Eldred, Matt Barone, John Jakeman, and Stefan Domino, and at Purdue University, we have Prof. Dongbin Xiu as our main collaborator.

The overall objective of this project was to develop a novel, comprehensive methodology for uncertainty quantification by combining stochastic expansions (nonintrusive polynomial chaos and stochastic collocation), the adjoint approach, and fusion with experimental data to account for aleatory and epistemic uncertainties from random variable, random field, and model form sources. The expected outcomes of this activity were detailed in the proposal and are repeated here to set the stage for the results that we have generated during the time period of execution of this project:

1. The rigorous determination of an **error budget** comprising numerical errors in physical space and statistical errors in stochastic space and its use for optimal allocation of resources;
2. A considerable increase in efficiency when performing uncertainty quantification with a **large number of uncertain variables in complex non-linear multi-physics problems**;
3. A solution to the **long-time integration** problem of spectral chaos approaches;
4. A rigorous methodology to account for **aleatory and epistemic uncertainties**, to emphasize the most important variables via **dimension reduction** and **dimension-adaptive refinement**, and to support fusion with experimental data using **Bayesian inference**;
5. The application of novel methodologies to **time-dependent reliability studies in wind turbine applications** including a number of efforts relating to the uncertainty quantification in vertical-axis wind turbine applications.

In this report, we summarize all accomplishments in the project (during the time period specified) focusing on advances in UQ algorithms and deployment efforts to the wind turbine application area. Detailed publications in each of these areas have also been completed and are available from the respective conference proceedings and journals as detailed in a later section.

In the UQ algorithms area, we have focused on scalability and robustness of core stochastic machinery, managing multiple model forms, and balancing deterministic and stochastic errors. Within the core stochastic machinery, we have explored adaptive p- and h-refinement along with adjoint gradient enhancement using either structured or unstructured grid approaches. We have also developed capabilities for multifidelity UQ that leverage less expensive low-fidelity models while seeking accurate high-fidelity statistics. Finally, we have demonstrated the use of adjoint-based error estimation for estimating components of spatial, temporal, and stochastic discretization errors within an error balancing framework.

In the wind simulation area, we have explored both low-fidelity and high-fidelity simulation tools for analyzing the performance of wind turbines. In the low-fidelity case, we have demonstrated the use of advanced UQ propagation methods and uncovered the need for methods that are robust with respect to nonsmooth behavior. In the high fidelity case, we are developing time spectral and sliding mesh discontinuous Galerkin approaches that will ultimately replace the low-fidelity approaches and allow us to assess performance and reliability in more challenging operating regimes.

2 Introduction

Wind turbine reliability plays a critical role in the long-term prospects for cost-effective wind-based energy generation. The computational assessment of failure probability or life expectancy of turbine components is fundamentally hindered by the presence of large uncertainties in the environmental conditions, the blade structure, and the physical models chosen to simulate the systems. Rigorous quantification of the impact of such uncertainties can fundamentally improve the state-of-the-art in computational predictions and, as a result, aid in the design of more cost-effective devices.

3 UQ Algorithms

In the sections below, we summarize our activities in UQ algorithm research and development. We organize around some of the key challenges in the UQ field, including scalability and robustness of core stochastic machinery, managing multiple model forms, and balancing deterministic and stochastic errors.

3.1 Scalability and robustness

Consider a set of uncertainties represented using a set of (independent) random variables $\xi_1, \xi_2 \dots \xi_d$ defined over a tensor space $\Omega = \Omega_1 \times \Omega_2 \times \dots \Omega_d$ and a quantity of interest $f(\xi_1 \dots \xi_d)$. In many engineering applications, the objective is to characterize the statistics of f, such as the mean and the variance which are defined as integrals over Ω, i.e.

$$E[f] = \int_\Omega f(\xi_1 \dots \xi_d) p_{\xi_1} p_{\xi_2} \dots p_{\xi_d} d\xi_1 d\xi_2 \dots d\xi_d,$$

where p_{ξ_k} represents the probability density function of the random variable ξ_k. One central challenge in uncertainty quantification algorithm development is the development of methods that are accurate in computing the statistics of f while only requiring a few function evaluations over the domain Ω.

Polynomial chaos expansions (PCE) represent f as a (truncated) series in an orthogonal polynomial basis and obtain the statistics directly in terms of the expansion coefficients f_k.

$$f(\xi_1 \dots \xi_d) \approx \sum_{k=0}^{P} f_k \pi_k(\xi_1 \dots \xi_d).$$

Stochastic collocation (SC) methods, on the other hand, directly address the computation of the statistics of f using quadrature rules and form multidimensional interpolants using a linear combination of function values at quadrature points and interpolation polynomials:

$$f(\xi_1 \dots \xi_d) \approx \sum_{k=1}^{N_p} f(\xi_1^k \dots \xi_d^k) L_k(\xi_1 \dots \xi_d).$$

Although widely successful, these methods suffer from exponentially increasing cost as d increases (*curse of dimensionality*) and limited accuracy when f is not sufficiently smooth. To address the dimensionality challenge, we have explored the use of (1) adaptive refinement methods that adjust polynomial orders (p-refinement) in different dimensions or regions according to suitable error estimates, (2) adjoint gradients to enhance function evaluations, and (3) sparsity detection techniques to limit the number of expansion coefficients required to achieve a given accuracy. The nonsmoothness challenge is typically handled using appropriate subdivisions of the domain Ω in an adaptive process similar to h-refinement in finite elements.

3.1.1 Polynomial chaos and stochastic collocation on structured grids

Adaptive refinement of stochastic expansions seeks to preferentially refine in the dimensions or regions of the stochastic domain Ω that are more important for resolving statistical quantities of interest (QOI). By investing computational effort where it is most needed, the scalability of the stochastic algorithm can be significantly improved when the relevant response metrics possess anisotropy or locality.

Initial refinement capabilities within DAKOTA focused on dimension-adaptive p-refinement within PCE and SC by controlling the orders of global basis polynomials used in different stochastic dimensions. These p-refinement approaches included: (1) uniform refinement using isotropic grids, (2) adaptive refinement using anisotropic grids, and (3) goal-oriented adaptive refinement using generalized sparse grids. These capabilities target improved scalability for smooth problems, for which global basis functions can be the most effective [10].

During the research conducted in this project, these refinement capabilities were extended to include dimension-adaptive h-refinement using local basis functions of fixed order, either linear or cubic spline basis polynomials (see Figure 2 in Section 3.1.3). We also focused on adding capabilities for hierarchical interpolation in SC, which both improve precision in dimension-adaptive approaches and enables new capabilities for local adaptive refinement. Local error estimates computed from hierarchical surpluses are used to guide local refinement within the framework of generalized sparse grids [16] using either local or global interpolation polynomials. The ability to perform local refinement provides a much finer grain of control than dimension-adaptive refinement, allowing for improved performance in applications that exhibit local response features. And the ability to employ local basis functions is critical for mitigating the effects of nonsmoothness.

3.1.2 Polynomial chaos on unstructured grids

The use of tensor (or sparse) constructions in the parametric space provides limited opportunities for adaptivity. Borrowing ideas from unstructured grid generation techniques we have developed a simplex based multi-element polynomial reconstruction technique with both h- and p-refinement capabilities. The h-refinement is achieved via random point-insertion in selected simplex elements having either large approximation error (based on hierarchical surplus error estimate) or large probability weight. The p-refinement is constructed including neighboring nodes [43]. This approach is effective in representing strongly non-linear or discontinuous response surfaces, provide a natural support for correlated uncertain variables and scales reasonably well for up to 10-dimensional spaces.

3.1.3 Adjoint enhancement

Two approaches have been pursued for adjoint enhancement in this project. First, polynomial regression for PCE can be readily adapted to include additional derivative matching conditions. In this straightforward implicit approach, matrix conditioning can be a limiting factor (Figure 1(a)) leading to increased solution error with higher-order bases (Figure 1(b)). Second, a novel approach for gradient-enhanced interpolation has been developed [9] in which type 1 and type 2 interpolation polynomials are employed to explicitly interpolate value and derivative data:

$$f(\boldsymbol{\xi}) \cong \sum_{j=1}^{N_p} \left[f_j \boldsymbol{H}_j^{(1)}(\boldsymbol{\xi}) + \sum_{k=1}^{n} \frac{df_j}{d\xi_k} \boldsymbol{H}_{jk}^{(2)}(\boldsymbol{\xi}) \right] \tag{1}$$

While global Hermite interpolation polynomials have exhibited instability during basis generation (Figure 1(c)), local cubic splines are stable. Figure 2 compares the use of local linear interpolants and cubic Hermite spline interpolants for smooth and nonsmooth test problems, in which the preference for global basis polynomials in smooth problems and for local basis polynomials in nonsmooth problems is evident.

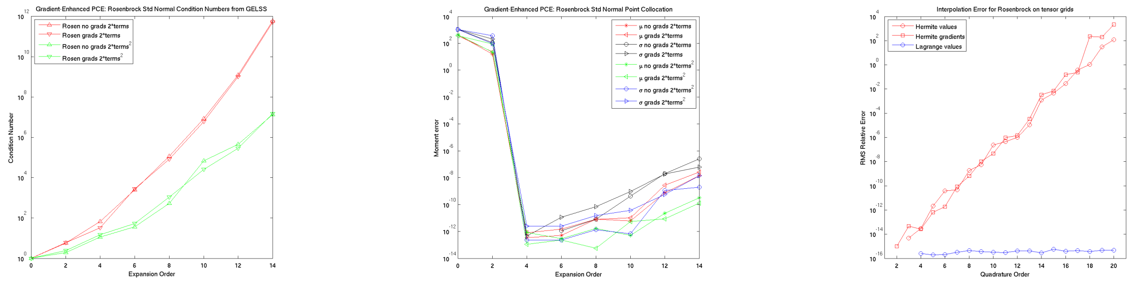

(a) Regression PCE: ill-conditioning. (b) Regression PCE: loss of accuracy. (c) Global Hermite SC: basis generation instability.

Figure 1: Ill-conditioning and instability in gradient-enhancement.

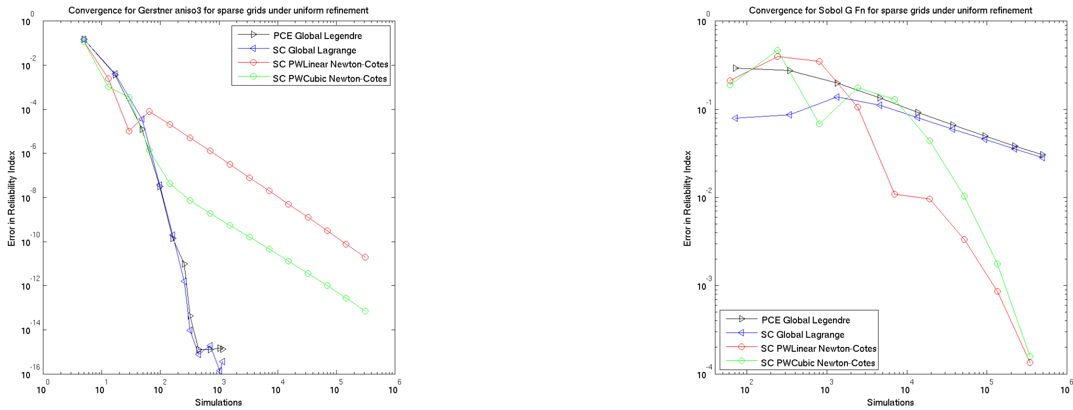

(a) Smooth. (b) Nonsmooth.

Figure 2: Comparison of convergence rates for global and local basis functions.

In addition, recent efforts in local h-refinement and compressive sensing are also targeting the inclusion of local adjoint-gradient information for informing global stochastic approximations formed in high dimensions. In the former case, this involves hierarchical gradient surpluses, and in the latter case, this involves inclusion of gradient matching conditions within L1 error minimization approaches.

3.1.4 Structured vs. unstructured polynomial chaos

A comparison between structured sparse grids (SG, with global uniform or local uniform/adaptive refinement) and unstructured stochastic simplex collocation (SSC with uniform/adaptive refinement) methods has been carried out for a number of analytical test functions. Two examples are reported in Fig. 3. The first one corresponds to the Rosenbrock function defined as $f(\xi_1, \xi_2) = 100(\xi_2 + \xi_1^2)^2 + (1 - \xi_1^2)$ while the second is Sobol's g-function: $g(\xi_1, \xi_2) = |4\xi_1 - 2|(|4\xi_2 - 2| + 1)/2$. In both cases ξ_1 and ξ_2 are two i.i.d. uniform random variables. The results show the convergence of various methods in terms of the error in the expected value of f and g by using an increasing number of function evaluations to build the response.

3.1.5 New direction: compressive sensing methodology

Work was also initiated in a compressive sensing approach that targets computation of the sparsest polynomial chaos basis representation given limited sample data and specified accuracy constraints. Initial investigations

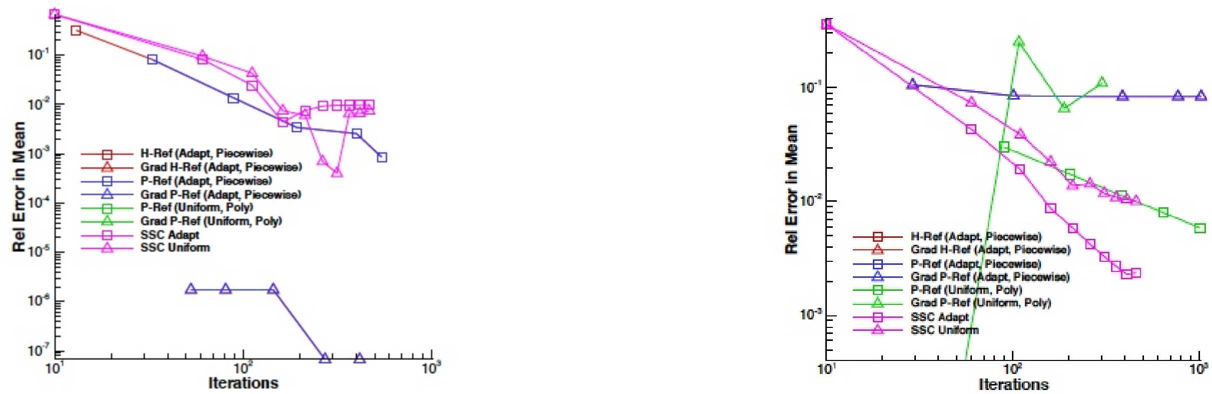

(a) Rosenbrock.

(b) Sobol.

Figure 3: Convergence comparison for structured and unstructured UQ methods on analytical test functions.

have identified the Approximate Message Passing (AMP) algorithm [6] as a viable and competitive approach for solving L1 minimization problems. This technique was also compared with more traditional Basis Pursuit algorithms [38].

3.2 Handling multiple model forms

Issues of model form are prevalent in wind turbine simulation. Production simulations are needed for use in industry that have fast turnaround on workstation-class compute resources. These tools are quite useful within the regimes for which their simplifying approximations are valid, but new questions regarding turbine reliability, fatigue, and failure require higher fidelity tools that must account for more complex physics, such as models for predicting loads from turbulent boundary layers. This situation highlights two distinct situations involving model form: (1) there is a clear hierarchy of low and high fidelity (e.g., the tools described in Section 4), or (2) there exists an ensemble of models (e.g., turbulence models for RANS or LES) that, in the absence of sufficient data to perform model selection, contribute additional epistemic uncertainty.

3.2.1 Multifidelity UQ

In the former case of a hierarchy of model fidelity, the UQ problem can be posed as one for which we seek statistics for the high fidelity (HF) model, but wish to leverage the less expensive low fidelity (LF) model to reduce the number of HF simulations and thereby reduce the overall expense of the study.

By forming a separate stochastic model for the discrepancy between LF and HF predictions, we can develop a highly-resolved stochastic model of the LF model due to its lower cost and then utilize a much lower resolution model of the discrepancy ($N_{hi} << N_{lo}$):

$$\hat{f_{hi}}(\boldsymbol{\xi}) = \sum_{j=1}^{N_{lo}} f_{lo}(\boldsymbol{\xi}_j)\boldsymbol{L}_j(\boldsymbol{\xi}) + \sum_{j=1}^{N_{hi}} \Delta f(\boldsymbol{\xi}_j)\boldsymbol{L}_j(\boldsymbol{\xi}) \tag{2}$$

When the model discrepancy has lower complexity than the original HF model, then the multifidelity convergence rate is accelerated, and when the variance of the discrepancy is reduced relative to the HF variance, then the initial error is reduced (the convergence trajectory is offset). In addition, the adaptive refinement approaches of Section 3.1.1 can be tailored for multifidelity problems. In particular, greedy adaptation can be applied to refinement of either of the two terms on the right hand side of Eq. 2, with normalization by relative cost. Then the candidate low fidelity or discrepancy increment that produces the greatest normalized benefit in the statistical QOI is selected by the adaptation. Refer to [25] for full details.

More details are provided in a later section of this final report.

3.3 Balancing errors

In pursuing high fidelity UQ, an error budget has been developed that includes contributions from limited numerical accuracy in spatial and temporal discretization and incomplete characterization/propagation of uncertainties. Discretization errors are estimated using adjoint-based methods [7], whereas errors in uncertainty propagation is controlled using adaptive refinement. Based on these estimates, a decision-making tool guides whether to invest additional resources in uncertainty resolution or spatial/temporal mesh refinement.

Since the aleatory uncertainty samples and the numerical discretization errors in these samples are both inputs to the error balancing process, the aleatoric UQ step provides the most suitable location to perform the decision making. For the aleatoric UQ, we employ the Simplex Stochastic Collocation [43] method which uses a multi-element discretization of the aleatoric parameter space based on simplex subdomains. The global uncertainty error estimate is composed as the sum of local contributions within each simplex element, and for each aleatoric sample, the spatial and temporal discretization errors are also evaluated. Starting with a few samples in stochastic space, the spatial, temporal, and stochastic discretization errors are determined and the largest contribution to the error is reduced until the total error falls below the desired threshold.

4 Wind turbine simulations

Existing low-fidelity wind simulation tools have provided an essential capability for rapid exploration of UQ methodologies within the target application domain. During the first year of this project our efforts focused on the setup of new UQ algorithms using these low fidelity tools as an initial testbed.

The computation of wind turbine loads and performance requires the development of comprehensive multi-physics codes that represent the blade aerodynamics, structural deformations, noise generation, environmental conditions, etc. We have leveraged existing tools developed by the National Renewable Energy Laboratory (NREL) and Sandia. The NREL aero-elastic code FAST, which predicts the wind turbine aerodynamic performance, loadings, and structural dynamics during operation in a variety of wind conditions, has been the primary design code in several of these studies. We have also developed a Matlab-based driver, called EOLO (described in detail in last year's report), to integrate FAST with other physics modules. These low-fidelity tools have been applied to representative wind turbine design and analysis problems incorporating UQ. In addition, Sandia's CACTUS suite of tools have also been leveraged for some of the calculations in this work.

In addition to low-fidelity tools, a variety of high-fidelity tools have been deployed to the project as a mechanism to evaluate the validity of the low-fidelity tools. These tools include the use of time-spectral methods and non-conformal sliding mesh algorithms using overset meshes.

4.1 Low fidelity: FAST, CACTUS

4.1.1 FAST 1.5 MW HAWT with steady inputs

In the first representative design problem, we consider a 1.5 MW utility-scale wind turbine operating in a steady wind (no turbulence) with a sheared wind profile. The wind shear gives rise to cyclical aerodynamic loads on the blades at a once-per-revolution frequency, as shown in Figure 4(b). In this case, the single uncertain parameter of interest is the wind shear, the magnitude of which is given by a shear exponent. The response function of interest is the amplitude of oscillation of the per-rev blade root bending moment. This is a simple surrogate for fatigue loading of an actual wind turbine blade in a real environment. Long-term meteorological data from a Great Plains wind site [42] were used to generate a distribution for the wind shear exponent (Figure 4(a)). This distribution is bi-modal, with two strong peaks appearing in the density function corresponding to unstable (by day) and stable (by night) atmospheric boundary layer conditions.

Figure 5 shows computational results for applying polynomial chaos expansion methods in DAKOTA to the FAST 1.5MW model with uncertain wind shear, where it is evident that PCE obtains comparable PDF/CDF results to 10^5 LHS samples at much lower cost ($O(10^1 - 10^2)$ samples) and that the numerically-generated orthogonal polynomial basis capability outperforms standard Wiener-Askey PCE approaches.

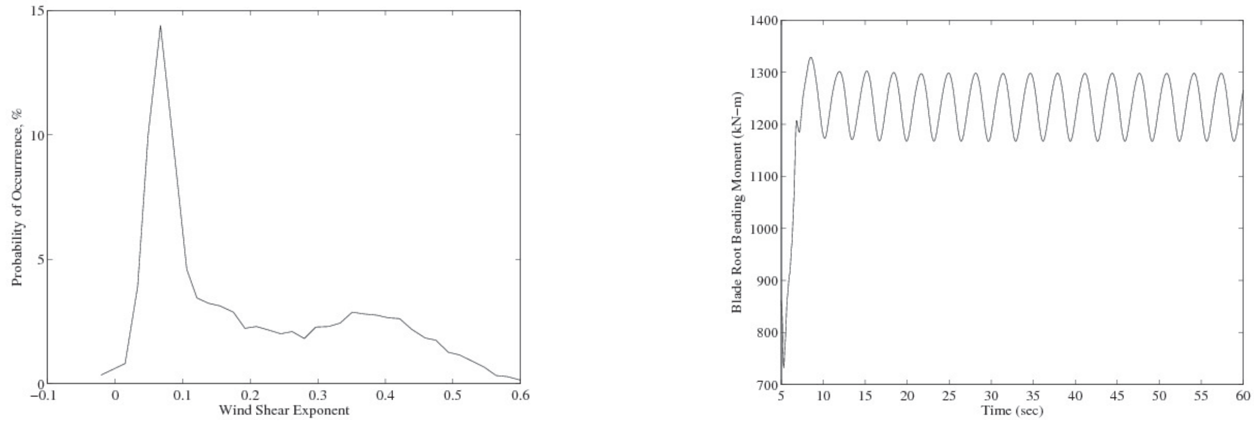

(a) Wind shear probability distribution.

(b) Time history of simulated wind turbine blade root bending moment.

Figure 4: FAST 1.5 MW uncertain input parameter and representative simulation results.

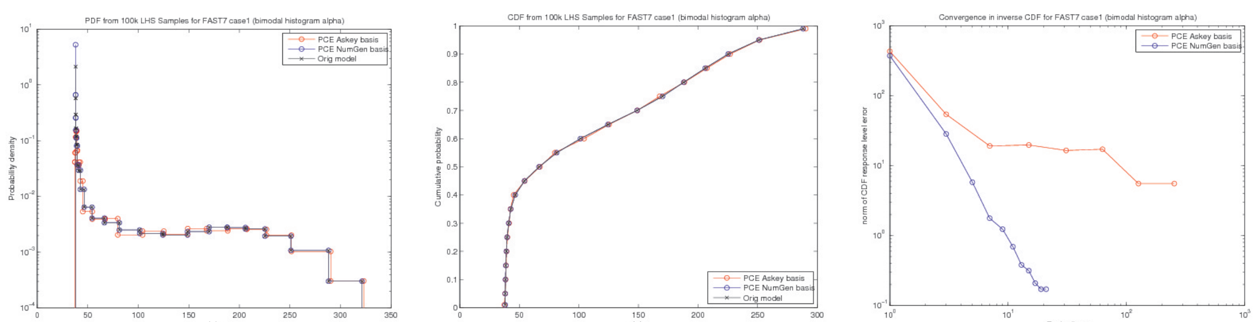

(a) Output PDF.

(b) Output CDF.

(c) Convergence rates for CDF.

Figure 5: Uncertainty quantification results for the FAST 1.5 MW HAWT with bimodal wind shear input.

4.1.2 FAST 1.5 MW HAWT with turbulent inputs

An important design driver for modern wind turbines is the fatigue loading resulting from turbulent wind inflow. This design case is analyzed by performing a limited number of aero-elastic simulations with excitation by a set of turbulent wind fields. This limited set of simulations is then used to estimate fatigue damage over the entire life time of the turbine. We have set up a representative fatigue design problem using the same 1.5 MW FAST model, but now operating within a modeled turbulent wind field. Initial results indicate the presence of substantial noise in the fatigue damage response function, which is due to statistical error from the limited amount of simulation performed. We also investigated UQ methods that remain robust with respect to such non-smooth response functions [30].

4.1.3 CACTUS VAWT

An aerodynamic model for a horizontal-axis wind turbine is necessarily three-dimensional, since it is comprised of two or three blades rotating about an axis parallel to the oncoming wind. A vertical-axis turbine (VAWT), where the axis of rotation is normal to the wind vector, allows for a meaningful two-dimensional analysis of one cross-section of the rotor. This makes the VAWT a useful bridging problem for investigation of UQ methods employing high-fidelity simulation, since methods can be developed and verified using 2D problems before extension to 3D. The VAWT has also been chosen as a testbed problem for multi-fidelity UQ methods. In this case, the low-fidelity tool is CACTUS (Code for Axial and Crossflow TUrbine Simulation). CACTUS is a three-dimensional potential flow code developed as Sandia that uses a lifting line/free-wave formulation to generate predictions of rotor performance and unsteady blade loads.

4.2 Low fidelity: EOLO

The non-intrusive UQ algorithms presented above have been used in combination with EOLO to study the effect of uncertainties in the wind conditions on the operating performance of a realistic 50kW wind turbine in terms of power coefficient and overall noise level [31]. Three uncertain parameters are considered, corresponding to wind velocity, turbulence intensity and wind angle; probability distributions associated with these parameters are defined in terms of histograms constructed from actual wind measurements.

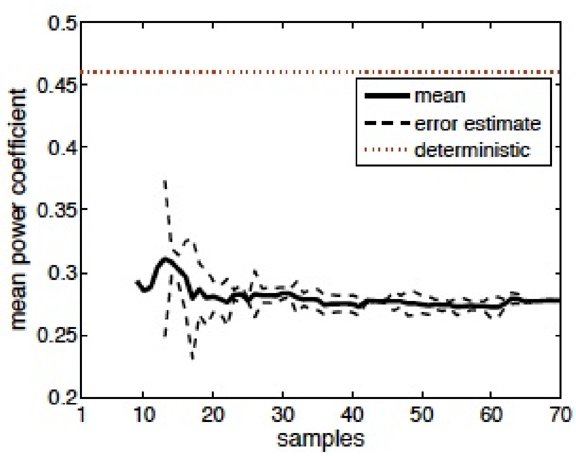

(a) Power coefficient.

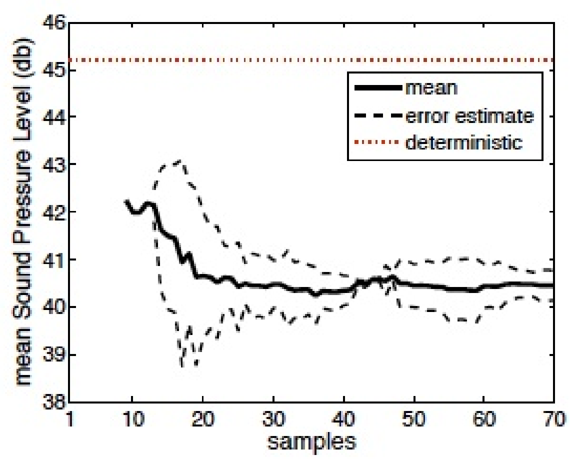

(b) Noise.

Figure 6: Effect of wind conditions variability on the performance of a 50kW wind turbine [31].

The results show that the performance penalty introduced by the uncertainties is considerable: up to 50% and 10% in terms of aerodynamic performance and noise respectively. More importantly the UQ methodology applied (the simplex collocation) provides a quantification of the effects of the uncertainties (and a corresponding error estimate) requiring only few EOLO solutions.

4.3 High fidelity: time-spectral URANS

High-fidelity simulations in the current project involve unsteady Reynolds Averaged Navier–Stokes (URANS) computations of VAWT flow fields. In our current approach, the temporal periodicity of VAWT flowfields is exploited and the time-integration process is simplified by the use of the time-spectral method [14]. In this approach, the time-derivative operation is replaced by a matrix-vector multiplication involving a mass-matrix that couples the discrete time-instances. This allows for a solution of the entire system of equations using standard steady-state acceleration techniques, and also simplifies the unsteady adjoint solutions.

For demonstration purposes, a single-bladed VAWT rotating at a corresponding Reynolds number of 67000 is considered. A tip-speed ratio (ratio of rotational velocity to free-stream velocity) of 7.5 is considered and the rotational radius to chord ratio is 4.0. This specific case has been chosen as it closely corresponds to measurements [59]. RANS simulation with the Spalart-Allmaras turbulence model is employed. Figure 7(a) shows the comparison of the time-spectral method (using 16 instances) with the full time marching method (second order backwards differencing) that uses 128 time-steps per period of revolution (and 7 revolutions before periodic steady state is achieved). The time-spectral method is seen to capture the essential features to a good level of accuracy. For this configuration, using a 64 instance time spectral method as a reference solution, the adjoint method was able to estimate 60% of the relative error (between the reference solution and the 16 instance solution). For purposes of validation, Figure 7(b) compares the present calculations to experimental measurements. It has to be mentioned that the present computations are two-dimensional, whereas the experiments used a short aspect ratio blade.

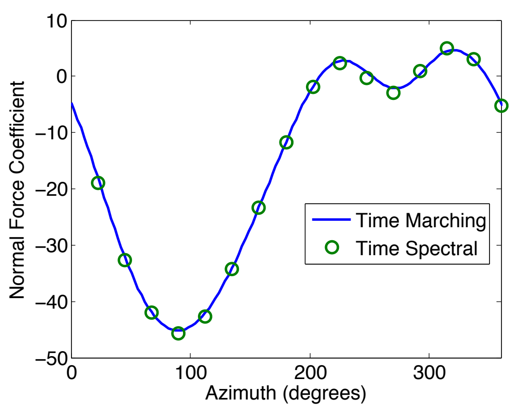

(a) Comparison of time-spectral and time-marching.

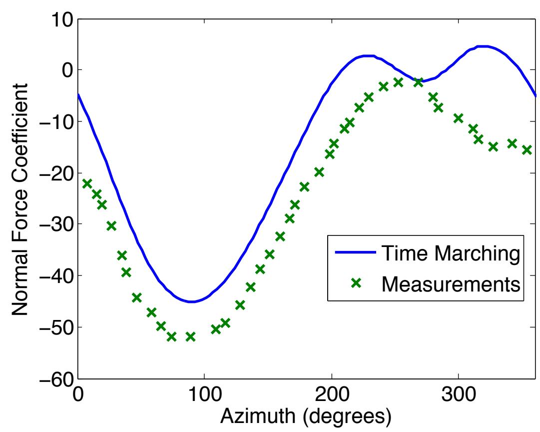

(b) Comparison of computation and experiments.

Figure 7: Comparison of Normal force coefficients.

4.4 High fidelity: SIERRA Mechanics

High fidelity simulations for wind energy applications inherently involve the requirement to solve the turbulent form of low Mach Navier Stokes equation set. The underlying mesh should be adequate to resolve the boundary layers on the blades all in the context of a rotating blade scenario. The core methodolody explored in the SIERRA Mechanics suite involves the use of sliding mesh boundaries between the inner VAWT mesh and the outer free stream mesh. The sliding mesh algorithm combines the Control Volume Finite Element method at interior domains with a discontinuous Galerkin (DG) implementation at the nonconformal mesh interface [5]. The low Mach number numerical scheme uses equal-order interpolation and a monolithic flow solver using explicit pressure stabilization. Details can be found in [5].

An initial proof of concept simulation study was performed for a VAWT geometry of interest to Sandia whereby the cross wind magnitude was varied in a fixed tip speed configuration of 40 m/s. Three different cross winds were used, 3, 5 and 8 m/s from which the integrated surface traction was computed (Fig. 8(b)).

The mesh outlining the three blade configuration along with the viscous surface traction at the leading edge for the three cross wind configurations are shown in Fig. 8(a). Efforts are now centered on transitioning the sliding mesh low Mach algorithm from a monolithic approach to a pressure projection scheme so that computational times can be reduced. Moreover, a VAWT validation case has been identified [36].

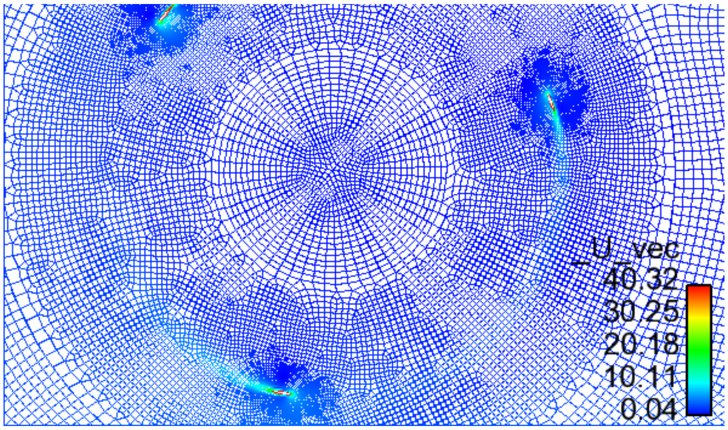

(a) Geometry

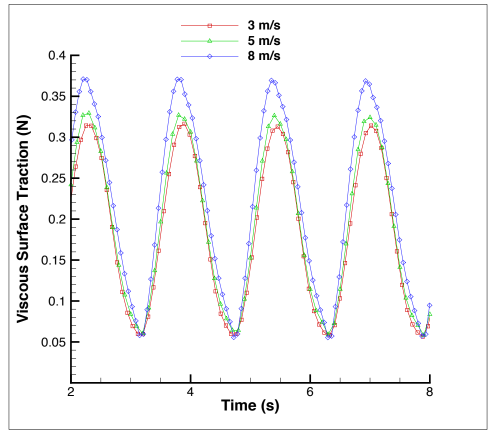

(b) Integrated viscous surface traction

Figure 8: SNL VAWT geometry and leading edge viscous surface traction for three cross wind velocities.

Sandia has continued the work that is related to this part of the overall effort and further details will be reported in their separate final report. No additional results related to the Sandia Large-eddy simulations are reported here.

5 Use of Adjoints for Spatial, Temporal, and Stochastic Error Estimation

Approaches to quantifying numerical error in the context of Finite Elements have been pursued for the past two decades [47, 48, 49], primarily with the objective of providing an indicator of the local contribution to the functional error. Pierce and Giles [50] presented a generic framework applicable to finite element/volume/difference based discretizations, that demonstrated super convergent functional estimates by adding a correction term based on the adjoint (or a dual) of the original governing equations. Venditti and Darmofal [51] proposed an algebraic equivalent of the Pierce and Giles [50] approach. This approach also utilizes the adjoint equations and the functional error on the baseline mesh is improved by computing an estimate of the functional on a refined mesh. The current work pursues the approach of Venditti and Darmofal because of its discrete nature, but extends it to the estimation, budgeting and control of spatial, temporal and stochastic errors.

Most wind turbine simulations result in unsteady periodic flows. The time-spectral method [52, 53] has proved to be efficient in the simulation of such flows. The basic idea of the time-spectral method is to have a Fourier representation of the time-derivative term of the unsteady flow equation to take advantage of the periodicity. When transformed back to the physical domain, the time derivative term appears as a high-order central difference formula coupling all the time levels. The solution can then be obtained by marching towards a steady-state in an auxiliary pseudo-time variable. One of the major advantages of the time-spectral method is that it makes the adjoint method applicable to unsteady flow simulations. In addition, the error estimation procedure of Venditti and Darmofal can be easily extended to time refinement. Hence, the current work will use this approach.

Duraisamy et al. [54] proposed a framework based on the use of adjoint equations to formulate an adaptive sampling strategy for uncertainty quantification for problems governed by algebraic or differential equations involving random parameters. The approach makes use of discrete sampling based on collocation on simplex elements in stochastic space. Adjoint or dual equations are introduced to estimate errors resulting from the inexact reconstruction of the solution within the simplex elements.

The current work attempts to carefully evaluate the aforementioned error estimation strategies in spatial, temporal and stochastic space for wind turbine applications. Such estimates can help budget the computational resources towards improving accuracy in regions of high errors and provide a basis for adaptive sampling in stochastic space.

5.1 Flow Solver

The flow is computed with the compressible, multi-block, structured, cell-centered, parallel RANS flow solver SUmb (Stanford University multi-block), developed at Stanford University under the sponsorship of the Department of Energy's Advanced Simulation and Computing Program. The inviscid fluxes are discretized using an upwind scheme in combination with the approximate Riemann solver of Roe [55]. The overshoots in the MUSCL reconstruction are avoided by applying the Van Albada limiter. Time integration is performed using the time-spectral method described earlier. Convergence is accelerated using a multigrid strategy in combination with local time stepping and a 5-stage Runge Kutta time integration scheme.

5.2 Adjoint Formulation

Consider a system of discrete equations obtained by applying a numerical scheme to the partial differential equations governing the system, written in a compact form as:

$$R(U(\vec{x})) = 0, \tag{3}$$

where U represents the state vector of the unknowns in the space-time domain, $\vec{x} \in \Omega$, that has a dimension of $N_x \times N_y \times N_z \times N_t$, where N_x, N_y and N_z, are the spatial dimensions and N_t is the number of time-spectral instances. Let $f(U)$ be a functional of interest. The discrete adjoint equation can be written as:

$$\left[\frac{\partial R}{\partial U}\right]^T \Psi = -\left[\frac{\partial f}{\partial U}\right]^T, \tag{4}$$

where Ψ is the adjoint variable.

A discrete adjoint solver to solve the above system of equations was implemented in SUmb by Mader [56]. The system is solved using PETSc (the Portable, Extensible Toolkit for Scientific computation) [57] and their preconditioned GMRES solver.

5.2.1 Stochastic Expansions

The adjoint formulation was extended to stochastic spaces by Duraisamy et al. [54]. The governing equation in eqn. 3 can be rewritten as:

$$R(U(\vec{x}, \vec{\xi})) = 0, \tag{5}$$

where the quantity $\vec{\xi} \in \Omega_s$ represents the random/uncertain variables with dimension N_ξ. In the stochastic space, the mean of the functional is considered as the objective function and is given by the expression:

$$J(U) = \int_{\Omega_s} f(U) d\xi, \tag{6}$$

and the treatment of higher moments is straightforward within this framework. In order to compute the above integral, the random space Ω_s is divided into N_E simplex elements, consisting of N_S vertices. The stochastic problem is converted to a deterministic problem corresponding to the N_S realizations of the random variables and the objective function is computed by performing a quadrature on the simplex elements

$$J(U) = \sum_{i=1}^{N_E} \int_{E_i} f(U) d\xi, \tag{7}$$

where, E_i represents a division of the random space Ω_s into N_E simplex elements. Unfortunately, the random solution U is available only at the vertices of the simplex elements. In order to perform the quadrature, an approximation $\tilde{U}$ is constructed using the solution at the vertices of the simplex elements using finite element techniques.

5.3 Spatial and Temporal Error Estimation

Consider a baseline (or coarse) space-time domain Ω_H and a fine space-time domain Ω_h which can be obtained, for instance, by isotropically refining the baseline mesh or by increasing the number of time-spectral instances or by combining both space and time refinement. The goal of this approach is to obtain an accurate estimate of some functional $f(U_h)$ on the fine domain based on the time-spectral flow and adjoint solutions on the coarse domain. To enable this estimation, the flow and adjoint solutions computed on the coarse domain have to be interpolated onto the fine domain (the interpolations are represented by U_h^H and $I_h^H \Psi_H$, respectively). Assuming linearity and expanding the functional and residual about U_h^H,

$$\begin{aligned} f(U_h) &= f(U_h^H) + \left.\frac{\partial f}{\partial U}\right|_{U_h^H} (U_h - U_h^H), && (8) \\ R(U_h) &= R(U_h^H) + \left.\frac{\partial R}{\partial U}\right|_{U_h^H} (U_h - U_h^H). && (9) \end{aligned}$$

If a discrete numerical scheme can ensure (to machine precision) $R(U_h) = 0$, one can write

$$\begin{aligned} f(U_h) &= f(U_h^H) + \left.\frac{\partial f}{\partial U}\right|_{U_h^H} (U_h - U_h^H) + (I_h^H \Psi_H)^T \left[R(U_h) - R(U_h^H) + R(U_h^H)\right] \\ &= f(U_h^H) + \left[\left.\frac{\partial f}{\partial U}\right|_{U_h^H} + (I_h^H \Psi_H)^T \left.\frac{\partial R}{\partial U}\right|_{U_h^H}\right] (U_h - U_h^H) + (I_h^H \Psi_H)^T R(U_h^H). \qquad (10) \end{aligned}$$

Now, define the adjoint residual operator as

$$R^\Psi = \left.\frac{\partial f}{\partial U}\right|_{U_h^H} + (I_h^H \Psi_H)^T \left.\frac{\partial R}{\partial U}\right|_{U_h^H}. \qquad (11)$$

This leads to the expression derived by Venditti and Darmofal [51] for the estimate of numerical error:

$$\begin{aligned} f(U_h) &= f(U_h^H) + (I_h^H \Psi_H)^T R(U_h^H) + R^\Psi (U_h - U_h^H) \\ &= f(U_h^H) + \epsilon_{cc} + \epsilon_{re}. \qquad (12) \end{aligned}$$

In the above equation, the first two terms can be evaluated by post-processing the coarse domain flow and adjoint solutions, while the third term is not computable. For the error estimation to be accurate, it would be desirable for $|\epsilon_{re}|$, the *remaining* error term, to be small relative to $|\epsilon_{cc}|$, the *computable* error. A possible way of achieving this could via mesh adaptation and temporal refinement.

5.4 Stochastic Error Estimation

In computing the statistical average [58], the integral in eqn. 7 is approximated using a quadrature on simplex elements which is exact for polynomials of degree s,

$$J \approx \sum_{i=1}^{N_E} \sum_{j=1}^{N_q} w_{ij} f(U_{ij})) + O(\Delta\xi^{s+1}). \qquad (13)$$

For the purpose of clarity, the subscripts $(.)_{ij}$ will be used to denote the value of the quantity $(.)$ at the j^{th} Gaussian quadrature point in element i. The quantities f, U and R can depend explicitly on the stochastic variables without changing the formulation, but the dependence is not indicated for the purpose of clarity.

Note that U is known only at the vertices of the simplices, ξ_k, $k = 1, ..., N_s$. Using these vertex values of U, the solution can be reconstructed at the Gaussian points using either a linear or quadratic reconstruction technique. If the reconstructed flow and adjoint solutions are $\tilde{U}$ and $\tilde{\Psi}$, respectively, and assuming linearity,

$$f(U_{ij}) = f(\tilde{U}_{ij}) + \frac{\partial f}{\partial U}(\tilde{U}_{ij})(U_{ij} - \tilde{U}_{ij}). \tag{14}$$

Since $R(U_{ij}) = 0$, then

$$\begin{aligned} f(U_{ij}) &= f(\tilde{U}_{ij}) + \frac{\partial f}{\partial U}(\tilde{U}_{ij})(U_{ij} - \tilde{U}_{ij}) + \tilde{\Psi}_{ij}^T \left[R(U_{ij}) - R(\tilde{U}_{ij}) + R(\tilde{U}_{ij})\right] \\ &= f(\tilde{U}_{ij}) + \tilde{\Psi}_{ij}^T R(\tilde{U}_{ij}) + \left[\frac{\partial f}{\partial U}(\tilde{U}_{ij}) + \tilde{\Psi}_{ij}^T \frac{\partial R}{\partial U}(\tilde{U}_{ij})\right](U_{ij} - \tilde{U}_{ij}) \\ &= f(\tilde{U}_{ij}) + \epsilon_{cc} + \epsilon_{re}. \end{aligned} \tag{15}$$

Note that the procedure mirrors the spatial error estimation procedure of Venditti et al. [51]. The first two terms in the above equation are computable, while the third term is not. If the remaining error is small, the mean value of the functional is given by

$$J \approx \sum_{i=1}^{N_E} \sum_{j=1}^{N_q} w_{ij} \left\{ f(\tilde{U}_{ij})) + \tilde{\Psi}_{ij}^T R(\tilde{U}_{ij}) \right\}. \tag{16}$$

5.5 Sample Results

The primary test case chosen for the validation of the described procedure is the experimental setup of Oler et al. [59]. The setup consists of a one-bladed vertical axis wind turbine operating in a water tank. The blade uses a NACA0015 airfoil and has a chord length of 15.24cm. The rotor diameter is 122cm, making the chord to radius ratio (c/R) to be 0.25. The rotor operates at a tip speed of 45.7cm/s, yielding a blade Reynolds number of 67000. Measurement were made at three different tip to wind-speed ratio (TSR) of 2.5, 5.0 and 7.5. The schematic of the flow is shown in Fig. 9(a).

Simulations are performed at a TSR of 7.5 in 2D. To avoid issues with low Mach number simulation using the compressible solver, the rotational Mach number is set to 0.225 (which is still in the incompressible regime). Therefore, the freestream Mach number is 0.03. The baseline grid used for the simulation is a

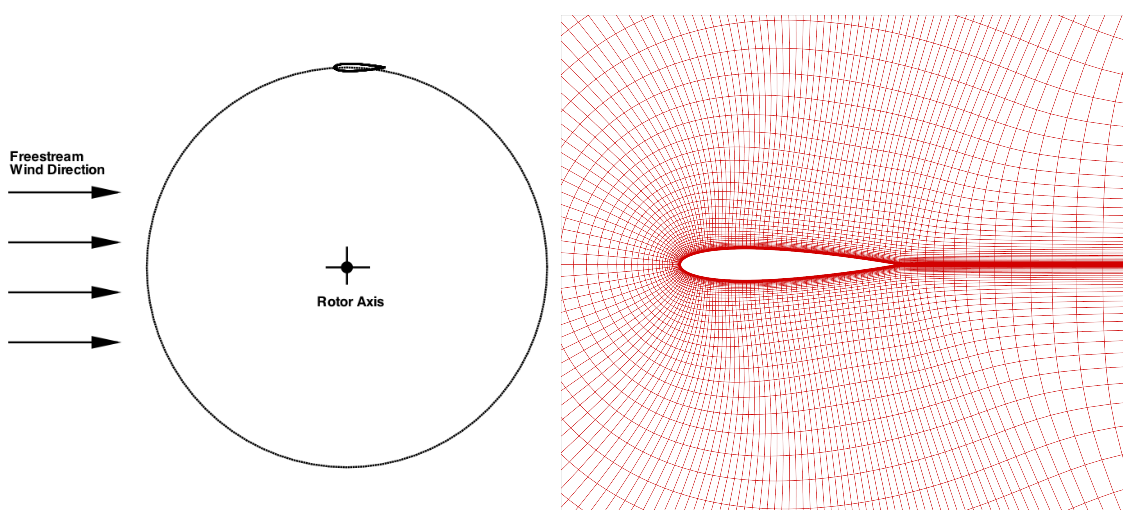

(a) Flow schematic (b) Mesh

Figure 9: Flow schematic and computational mesh for vertical axis wind-turbine calculation.

C-type grid with 229×65 points and is shown in Fig. 9(b). Simulations are also done on a grid that is refined in both directions to verify the error estimation.

5.5.1 Flow Solver Verification and Validation

Figure 10 shows the comparison of the predicted normal and tangential force coefficients as a function of azimuth with the experimental data. Shown are the results from inviscid and viscous simulations. The normal force predicted by the CFD is within 10% of the experimental value for both viscous and inviscid calculations. On the other hand, as expected the tangential force prediction has higher discrepancy using the inviscid calculation. However, since the focus of this initial effort is on numerical error estimation, the inviscid setup should serve a good first step for basic validation of the error estimation procedure.

In Fig. 11, the results from time spectral calculation are compared against those of the time marching calculation. The inviscid results using 16 and 32 time-spectral intervals, as well those from the time marching simulation using 256 time steps are shown. Clearly, the time spectral solution is seen to converge to the time marching result when the number of time instances is increased.

5.5.2 Verification of Adjoints

To verify the adjoint solution, the sensitivity of the tangential force (averaged over one period) with respect to the freestream Mach number is computed using adjoints and compared with finite difference estimation. Table 1 compares the results obtained using 16 time-spectral intervals.

Average Tangential force (F_T)	dF_T/dM_∞	
	Adjoints	Finite difference
0.4324	43.9425	44.2016

Table 1: Comparison of sensitivities using adjoints and finite difference.

5.5.3 Error Estimation

Spatial Estimation

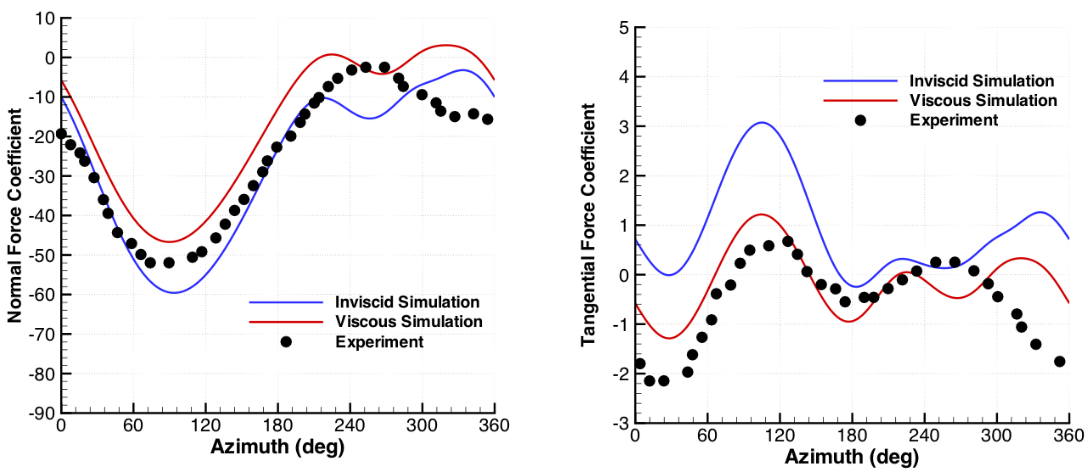

(a) Normal force coefficient

(b) Tangential force coefficient

Figure 10: Comparison of force time histories between CFD and experiment.

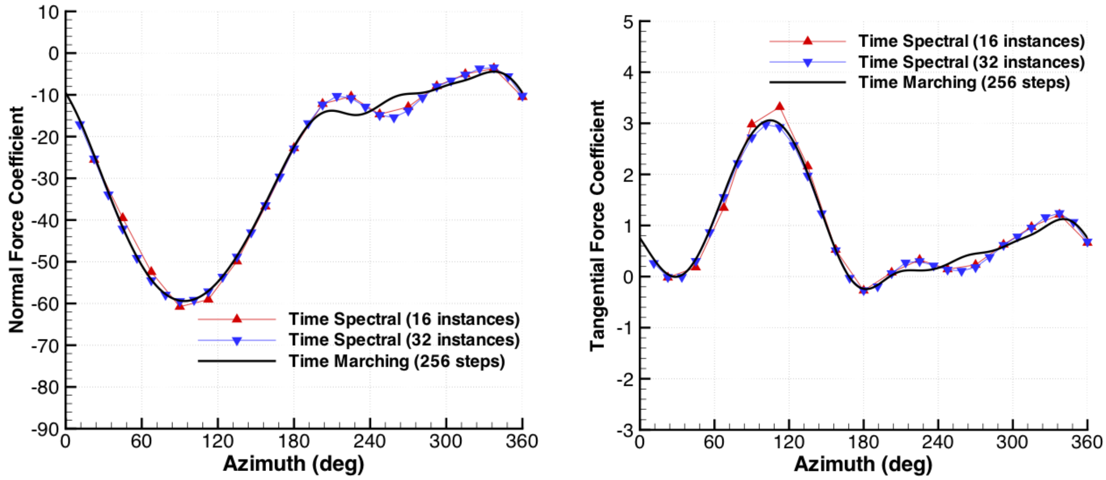

(a) Normal force coefficient

(b) Tangential force coefficient

Figure 11: Comparison of force time histories for different time spectral instances.

To verify the accuracy of the spatial error estimation approach, a steady flow at 10° angle of attack past the NACA0015 airfoil is considered for the initial verification. The flow is again assumed to be inviscid and the freestream Mach number is set to 0.15. The functional is chosen to be the lift coefficient and the error estimation is performed on two levels of grid refinement, the baseline grid being the same as that used for the Oler simulation. The results are shown in table 2. Clearly, the spatial error estimation is able to recover most of error arising due to inadequate spatial resolution.

	C_l	Error Estimate	% Actual Error
Baseline Grid	1.2223	0.0099	77.7
Fine Grid	1.2350	0.0019	125.3
Superfine Grid	1.2366	–	

Table 2: Spatial error estimation results on lift coefficient for steady flow past NACA0015 airfoil.

Spatial and Temporal Estimation

To verify the spatial and temporal error estimation, a simulation of the Oler case using 16 time-spectral intervals is used as a baseline. Both flow and adjoint solutions are obtained on this domain. To obtain a spatial error estimate, the baseline solution is interpolated onto a finer grid (refined in both directions), while keeping the number of time instances same. For temporal error estimation, the baseline solution is spectrally interpolated onto 32 time intervals, but the spatial grid is frozen. To obtain a combined space-time error estimate, the solution is interpolated both onto the fine grid and onto finer time intervals. The corresponding flow solution is simulated on the finer domain to verify the accuracy of the error estimates. Table 3 tabulates various spatial and temporal error estimation results on the average tangential force.

From table 3, it is seen that the temporal error estimation recovers only 12.36% of the actual error, while the spatial error estimation recovers 52.87% of the actual error. Interestingly, the combined space and time error estimation recovers 101.2% of the error. The space and time error estimation, while requiring more tests, is confirmed to be suitable to provide reliable adaptation indicators.

Stochastic Error Estimation

For an initial verification of the stochastic error estimation, the variation in wind speed is considered as the only random variable. The freestream velocity is allowed to vary in the Mach number range of 0.025 to 0.035. Note that the spatial and temporal error estimation was done at a freestream Mach number of 0.03. The mean value of the power is taken to be the objective function. To evaluate the objective function,

	Time Intervals	F_T	Error Estimate		
			Time	Space	Space & Time
Baseline Grid	16	0.4324	0.0113	0.4491	0.4602
	32	0.5238	-	-	-
Fine Grid	16	1.2818	-	-	-
	32	0.8871	-	-	-

Table 3: Spatial and temporal error estimation results on average tangential force.

flow solutions are obtained at 3 sampling points distributed uniformly in the above mentioned freestream range, as well as along the 5-point quadrature locations of the same range. In addition, adjoint solutions are obtained at the three sampling points. To obtain the error estimation, the flow and adjoint solutions from the sampling points are interpolated onto the 5-point quadrature locations using a spline fit.

Stochastic Integration	Value	Error Estimate
3-point	1.66247	4×10^{-4}
5-point	1.66286	-

Table 4: Stochastic error estimation results on power.

It is seen that the procedure is able to provide a good estimate of this small error magnitude, but further verification needs to be done for better confidence.

6 Multi-Fidelity UQ Application to a Vertical Axis Wind Turbine Under an Extreme Gust

Designing better vertical axis wind turbines (VAWTs) requires considering the uncertain wind conditions they operate in and quantifying the effect of such uncertainties. We study the effect of an uncertain extreme gust on the maximum forces on the blades of the VAWT. The gust is parametrized by three random variables that control its location, length, and amplitude. We propose a multi-fidelity approach to uncertainty quantification that uses polynomial chaos to create an approximation to the high-fidelity statistics via a correction function based on the difference between high and low-fidelity simulations. We found the proposed multi-fidelity method provides better estimates of maximum forces statistics with fewer number of high-fidelity simulations than those required by the high-fidelity method. Also, we developed a practical method to simulate a gust, in a CFD solver, that changes its magnitude in the flow direction by combining the field velocity method (FVM) and the geometric conservation law (GCL). The ability to study the effect of the gust with the high-fidelity (CFD) solver is crucial as the low-fidelity (blade element/vortex lattice) solver underestimates the effect of the gust on the maximum forces.

6.1 Introduction

Quantifying the response of a wind turbine to an extreme wind gust is an important design requirement[1]. The aerodynamics of the gust interacting with the turbine blades are complex and difficult to model because of dynamic stall[39]. Different simulation tools can be used to model the interaction of the gust with the turbine blades. These models can be classified as “high-fidelity” or “low-fidelity”. A high-fidelity model will accurately simulate the gust and blade interaction but at a high computational cost; whereas, a low-fidelity model will provide a less accurate simulation but at a low computational cost.

Low-fidelity tools are used extensively in the modeling of vertical axis wind turbines (VAWTs)[15, 34, 33] because of their low computational cost and relative good accuracy for normal operating conditions. However, their performance will be degraded in the presence of the gust[39].

In current practice, only a single "most likely" extreme gust event is simulated. Whereas, in reality, the extreme gust is stochastic[40, 20] and failure to account for the variability or uncertainty in the gust can lead to either over-conservative designs or, in some cases, under-design. Many simulations are needed to properly quantify the effect of the uncertain gust on the wind turbine. Using only a cheap low-fidelity model to perform the many simulations will likely not result in accurate statistics and relying exclusively on the high-fidelity model will give us accurate statistics but at a high cost.

Here we explore the use of multi-fidelity uncertainty quantification in order to reduce the computational cost of obtaining accurate statistics of the maximum forces on the wind turbine blades by combining a small number of high fidelity simulations with a large number of low-fidelity simulations (section 6.4.3). The multi-fidelity uncertainty quantification approach is similar to previous work in Ref. [24], but here we apply it to a more complex problem and for which the low-fidelity model is not a very good replacement of the high-fidelity model.

In this work, we consider a computational fluid dynamics (CFD) solver as the high-fidelity tool and a blade element/vortex lattice aerodynamic model as the low-fidelity tool. To the best of our knowledge we perform the first practical CFD simulation of an extreme wind gust with a wind turbine. This is done by combining the Field Velocity Method (FVM) with the Geometric Conservation Law (GCL) (section 6.3.1).

The uncertain gust and the vertical axis wind turbine considered in this problem are described in section 6.2. The the high and low-fidelity simulation tools are described in section 6.3.1. The uncertainty quantification method is described in section 6.4 and the results follow in section 6.5

6.2 Problem definition: The uncertain gust and the VAWT

For an extreme gust, the shape, size, and position are uncertain. Here we take the gust shape as fixed and treat the variables that determine the size and position of the gust in a probabilistic setting to properly determine the output distribution and statistics for the maximum loads. The extreme gust shape we use is the one specified in the IEC standard[1]

$$u_g(x) = \begin{cases} U_\infty - 0.37 u_e \sin\left(\frac{3\pi(x-x_0)}{L_g}\right)\left[1-\cos\left(\frac{2\pi(x-x_0)}{L_g}\right)\right], & \text{if } 0 \le x - x_0 \le L_g; \\ U_\infty, & \text{otherwise;} \end{cases} \tag{17}$$

where U_∞ is the average free-stream velocity, x_0 is the gust starting position, L_g is the gust length, and u_e is the gust amplitude. An example of this gust is shown in fig. 12.

6.2.1 Uncertain variables

For the fixed gust shape given by eq. (17), we treat its parameters (x_0, L_g, u_e) as uncertain variables that follow the probability distributions listed in table 5 and consider the mean wind speed U_∞ fixed at 8.5 m/s. For the particular turbine considered in this work (section 6.2.5 and table 6), the numerical values of the variables of the distributions are also listed in table 5, and the corresponding probability distribution functions are shown in fig. 13.

6.2.2 Gust starting position x_0

The gust starting position x_0 follows a uniform distribution in the interval $[-246.86\,\text{m}, -179\,\text{m}]$ that accounts for all possible interactions of the gust with the turbine blades. The $x = 0\,\text{m}$ position is at the turbine center of rotation.

6.2.3 Gust length L_g

The gust length L_g follows a normal distribution with mean $\mu_{L_g} = U_\infty T_g$, where the gust time scale ($T_g = 10.5\,\text{s}$) is the deterministic value given in the IEC standard. For the standard deviation, we picked a reasonable estimate of 10% of the mean value, $\sigma_{L_g} = 0.1\,\mu_{L_g}$.

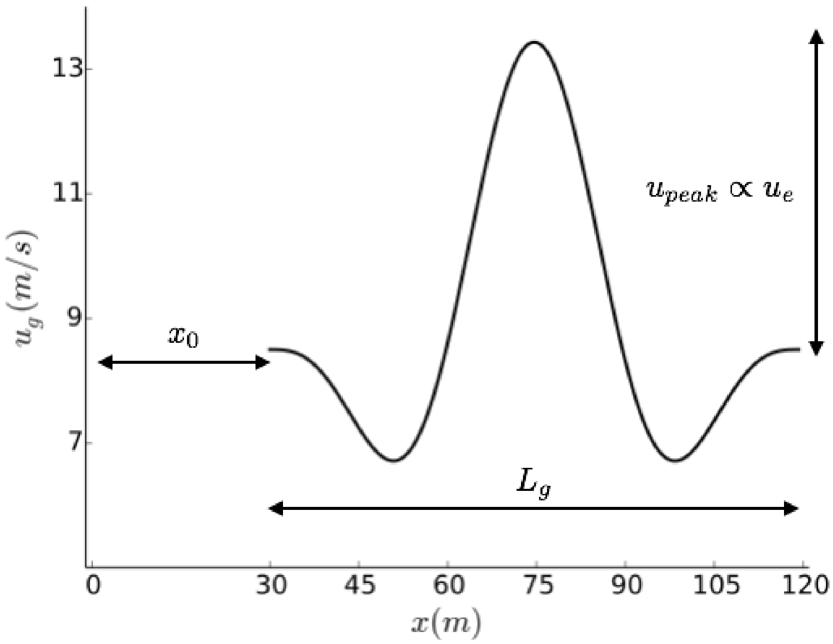

Figure 12: Example of an extreme gust with gust parameters (x_0, L_g, u_e).

Uncertain parameter	Probability distribution	Distribution variables
x_0	Uniform (a, b) $f(x_0) = \frac{1}{b-a}$	$a = -246.86\,\mathrm{m}$, $b = -179\,\mathrm{m}$
L_g	Normal (μ, σ) $f(L_g) = \frac{1}{\sqrt{2\pi}\sigma} e^{-\frac{1}{2}(\frac{L_g-\mu}{\sigma})^2}$	$\mu = 89.25\,\mathrm{m}$, $\sigma = 8.925\,\mathrm{m}$
u_e	Gumbel (α, β) $f(\zeta)^{\dagger}= \alpha \exp[-e^{-\alpha(\zeta-\beta)}]e^{-\alpha(\zeta-\beta)}$	$\alpha = 1.14$, $\beta = 11.24$

Table 5: Uncertain parameters for the extreme gust and their probability distributions. The values of the distribution variables are for the particular turbine considered in this work (see table 6).

† The gust amplitude is obtained from $u_e = \sigma_u \zeta$.

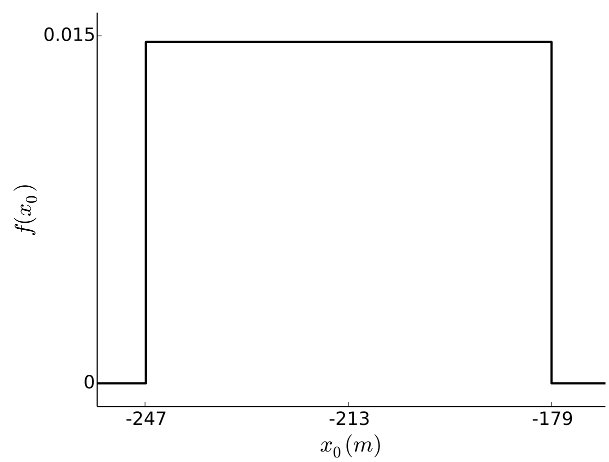

(a) Uniform distribution for the gust starting position.

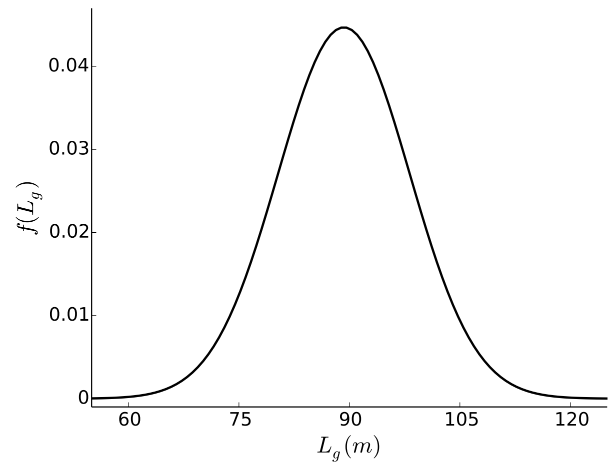

(b) Normal distribution for the gust length.

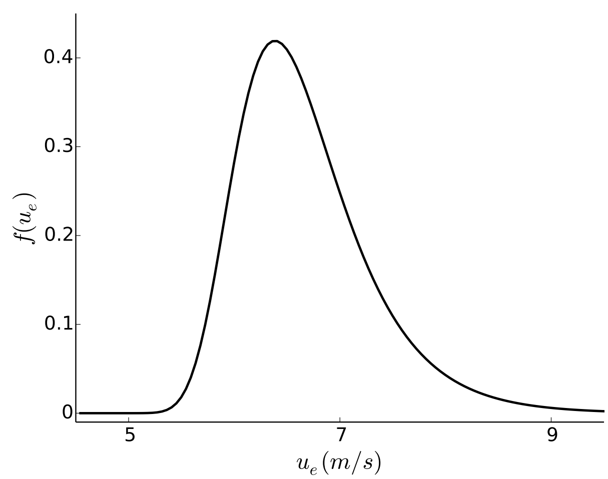

(c) Gumbel distribution for the gust amplitude.

Figure 13: Probability distributions for the uncertain variables.

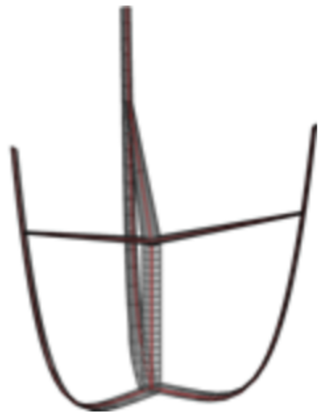

(a) The 5 MW VAWT.

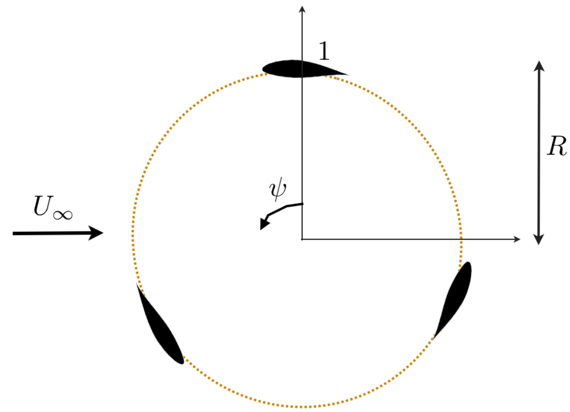

(b) A schematic of a 2D horizontal slice of the VAWT.

Figure 14: The vertical axis wind turbine and a schematic for the two-dimensional horizontal slice through the tips of the VAWT considered in this work.

6.2.4 Gust amplitude u_e

The gust amplitude u_e follows a gumbel distribution. This gumbel distribution can be derived from the wind climate given in the IEC standard as shown in detail in Larsen and Hansen[20]. Here we briefly describe how to obtain the parameters (α, β) that determine the Gumbel distribution,

$$f(\zeta) = \alpha \exp[-e^{-\alpha(\zeta-\beta)}]e^{-\alpha(\zeta-\beta)}, \quad \alpha = \frac{1}{2C(z)}, \quad \beta = 2C(z)\ln(T\kappa), \tag{18}$$

where $\zeta = {}^{u_e}/_{\sigma_u}$ is the gust amplitude normalized by the standard deviation of the wind velocity, and T is the recurrence period for an extreme gust. We set $T = 50$ years, which is a common value in wind turbine design. Expressions for the standard deviation of the wind velocity σ_u, the terrain and altitude dependent empirical constant $C(z)$, and the expected rate of local extremes κ, can be found in Larsen and Hansen[20]. These expressions depend on the particular geometry and operating conditions of the turbine. Using the turbine considered in this work (section 6.2.5 and table 6) we obtain the distribution variables listed in table 5 and the probability distribution for ζ and then u_e ($u_e = \sigma_u\zeta$) that is shown in fig. 13(c).

6.2.5 VAWT description

The wind turbine considered is a preliminary design generated at Sandia National Laboratories for a 3-bladed, 5 MW, offshore vertical-axis wind turbine (VAWT) (fig. 14(a)). The maximum rotor radius is 54 meters, and the rotor height measured from the bottom blade attachment point to the blade tips is 104.7 meters. A central tower extends from the rotor base to 70% of the rotor height, and is attached to the blades via three support struts. The present analysis considers a two-dimensional horizontal slice through the rotor at the blade tips (fig. 14(b)). This is the region of most interest from the aerodynamics perspective, given that this is the location where the maximum forces are generated per unit span. The blade chord at this location is 2 meters, with the blade attachment point located at 25% of the chord (measured from the leading edge). The airfoil section is a SNL 0018/50, a natural laminar flow airfoil developed specifically for VAWTs. The design RPM at rated power for this turbine is 7.4 RPM. A summary of the geometry and the operating conditions for the VAWT are listed in table 6.

6.3 Methods: Modeling the gust and uncertainty quantification

In this section we describe the two important ideas put forth in this paper 1) a practical method to simulate a wind gust for wind turbine applications in a CFD solver and 2) a multi-fidelity approach to uncertainty

Turbine data	Specification
Operating data	
Rated capacity (MW)	5
Terrain type	Offshore
Average wind speed U_∞ (m/s)	8.5
Reynolds number	5.4×10^6
Tip speed ratio λ	5
Geometry data	
Number of rotor blades	3
Rotor diameter (m)	108
Blade chord c (m)	2.00
Blade attachment point	$0.25c$
Height from base of rotor (m)	104.7
Airfoil	SNL 0018/50
Specific data to calculate u_e (section 6.2.4)	
Turbulence intensity I_{ref}	0.16
Reference wind speed U_{ref} (m/s)	37.5
Mean wind speed bin width (m/s)	2
Extreme gust recurrence period T (year)	50

Table 6: Vertical axis wind turbine description.

quantification. Also, we describe the low and high-fidelity tools used to simulate the wind turbine and we describe polynomial chaos, the uncertainty quantification method the proposed multi-fidelity approach uses.

6.3.1 Modeling of the gust interaction with the VAWT

The are many aerodynamic models available to simulate a wind turbine [15, 34, 33, 19, 22, 37], ranging from simple analytic models all the way to Direct Numerical Simulation (DNS), where each model depending on the context can be considered a high-fidelity or low-fidelity model. For this paper we consider the Euler equations in SU^2 (a CFD solver) as the high-fidelity model and CACTUS, a blade element/vortex lattice aerodynamic solver, as the low-fidelity model. The difference in simulation time between SU^2 and CACTUS (1 simulation takes 1 min on 1 processor) is around 3 orders of magnitude. These models are described below as well as how to model a gust in SU^2. The modeling of the gust in a CFD solver (SU^2) is not a straight forward task for this reason a subsection is devoted to introduce a practical method to model the gust. On the other hand modeling the gust in a low-fidelity tool such as CACTUS is straightforward, all that is needed is to modify the free-stream velocity as a function of time.

SU^2- High-fidelity model

The high-fidelity model is Stanford University Unstructured (SU^2)[27]. SU^2 is a C++ software suite developed for the specific task of solving partial differential equations (PDE) and PDE-constrained optimization problems on general unstructured meshes. The computational fluids dynamics (CFD) solver in SU^2 suite has been used and validated for many aerospace engineering applications[28].

In this work we use the compressible two-dimensional Euler equations to model the aerodynamics of the gust interacting with the vertical axis wind turbine. We use the Euler solver in SU^2 as opposed to the RANS solver, because of the cheaper computational cost without a significant loss of accuracy for our problem.

The Euler equations are solved on a domain $\Omega \subset \mathbb{R}^2$, with airfoil boundaries S and far-field boundary Γ_∞,

$$\begin{aligned} \partial_t U + \partial_x F + \partial_y G &= 0, && \text{in } \Omega, \\ (\vec{u} - \vec{x}_t) \cdot \vec{n}_S &= 0, && \text{on } S, \\ W_+ &= W_\infty, && \text{on } \Gamma_\infty, \end{aligned} \tag{19}$$

where

$$U = \begin{bmatrix} \rho \\ \rho u \\ \rho v \\ \rho E \end{bmatrix}, \; F = \begin{bmatrix} \rho(u - x_t) \\ \rho u(u - x_t) + p \\ \rho v(u - x_t) \\ \rho E(u - x_t) + pu \end{bmatrix}, \; G = \begin{bmatrix} \rho(v - y_t) \\ \rho u(v - y_t) \\ \rho v(v - y_t) + p \\ \rho E(v - y_t) + pv \end{bmatrix},$$

ρ is the fluid density, $\vec{u} = [u, v]^{\mathrm{T}}$ is the fluid velocity in a cartesian coordinate system, $\vec{x}_t = [x_t, y_t]^{\mathrm{T}}$ is the boundary velocity (mesh velocitiy after discretization), E is the total energy per unit mass, and p is the static pressure

$$p = (\gamma - 1)\rho \left(E - \frac{1}{2}(u^2 + v^2) \right).$$

The second line of eq. (19) represents the flow tangency condition at a solid wall, and the third line represents a characteristic-based boundary condition at the far-field where the fluid state at the boundary is updated using the state at infinity depending on the sign of the eigenvalues.

In the numerical implementation, the Euler equations eq. (19) are discretized using a standard edge-based finite volume formulation on the dual grid, obtained by applying the integral formulation of the equations to a dual grid control volume surrounding any given node of the grid and performing an exact integration around the outer boundary of this control volume. The convective flux is discretized using a central scheme with JST-type artificial dissipation.[18] Time integration is implicit and handled by a second-order accurate dual-time stepping approach.[17]

CACTUS - Low-fidelity model

The low-fidelity model is CACTUS, the Code for Axial and Crossflow Turbine Simulation developed at Sandia National Laboratories (SNL).[23] CACTUS simulates the performance and loads of a wind turbine rotor in the time domain using a blade element/vortex lattice aerodynamic model. The rotor blades are discretized into blade element sections, where each section is assigned two-dimensional airfoil performance characteristics in the form of tables containing lift, drag, and moment coefficient vs. angle of attack. CACTUS also incorporates unsteady aerodynamic blade load effects such as dynamic stall, apparent mass and blade rotation effects. For the wake flow field, CACTUS uses a potential flow model comprised of free vortex line elements shed and trailed from each blade element at each time step.

Gust modeling in a CFD solver (SU^2)

Modeling a wind gust in a CFD solver is non-trivial. Initializing the gust in the flow field or specifying the gust as a time-dependent boundary condition (this approach is used for the low-fidelity tool) will not work. The reason for this is that the specified gust should satisfy the Euler equations eq. (19) or at least the gust velocity field $\vec{V_g}$ should be divergence free $\nabla \cdot \vec{V_g} = 0$. The extreme gust, specified in the IEC standard, and considered here

$$\vec{V_g} = \begin{bmatrix} u_g(x) = eq.\ (17) \\ v_g = 0 \end{bmatrix}, \tag{20}$$

changes its magnitude in the free-stream direction and has non-zero divergence

$$\nabla \cdot \vec{V_g} = \partial_x u_g + \partial_y v_g = \partial_x u_g(x) \neq 0. \tag{21}$$

In the rest of this section we describe a practical method that will allow us to simulate a gust that changes its magnitude in the free-stream direction and whose velocity field has non-zero divergence.

Even though the wind turbine gust has non-zero divergence, there are divergence free gusts in aerospace applications and efficient methods to simulate them have been developed. Two examples are a gust whose magnitude changes are perpendicular to the free-stream, which is used for gust alleviation studies in aircraft and a vortex gust used to study blade vortex interactions that occur in rotorcraft. An efficient method used to study the effect of these divergence free gusts is the Field Velocity Method (FVM)[32, 29, 35, 46, 3]. This method prescribes the gust as grid velocities which alleviates the problem of needing small cells everywhere in the mesh in order to avoid the gust being dissipated. For a CFD code that already has the capability to simulate moving meshes what is needed is to specify the gust as the negative of the grid velocity in the Euler equations eq. (19), $x_t = -u_g$. Our case, has true grid velocities due to the rotation of the wind turbine, so for cases with true grid velocities $x_{t_{true}}$ we would set $x_t = x_{t_{true}} - u_g$.

Note that the FVM is not quite equivalent to the Euler equations because of the extra prescribed gust velocity. Also, as the gust velocity is prescribed, only the effect of the gust on the body is captured, whereas the effect of the body on the gust is not. As long as the body does not affect the source of the gust which is almost always the case and which is the case here, the FVM method works remarkably well [32, 29, 35, 46, 3].

Directly applying the FVM to the non-divergence free extreme gust causes non-physical behavior and the method fails terribly. Using the recently developed Split Velocity Method (SVM)[41] an extension to the FVM that captures the effect of the body on the gust by introducing additional source terms in eq. (19) also does not work to simulate the gust.

When performing simulation with dynamic meshes (grid velocities) it has been shown that Geometric Conservation Law (GCL)[4, 21, 11] should be satisfied for consistency in the governing equations. Usually adding GCL provides a slight improvement in accuracy.

Here we found that satisfying the GCL is crucial when using the FVM method, as this combination allows us to successfully simulate the extreme gust and in fact any non-divergence free gust. To our surprise combining the GCL with the SVM does not work.

In summary, a practical method to model a gust that changes magnitude in the free-stream direction (a non divergence free gust) requires the use of the field velocity method in combination with the geometric conservation law.

6.4 A multi-fidelity approach to propagating the gust uncertainty

Uncertainty quantification (UQ) is the process of 1) characterizing input uncertainties, 2) propagating these uncertainties through a computational model, and 3) quantifying the effect of the input uncertainties on the output(s) of interest. In essence, uncertainty quantification aims to gain a quantitative understanding of how variations in the inputs of a model affect the outputs. For instance, how do the uncertain gust parameters affect the maximum load on the turbine. The first step of characterizing the input uncertainties was done in section 6.2 and the last step of characterizing the output of interest is done in the results section (section 6.5). In this section, we describe a novel approach to the second step of propagating the uncertainties by using computational models of different fidelities.

Different methods for performing the propagation of the input uncertainties depend on the type of the input uncertainties, either epistemic or aleatory. Epistemic uncertainties are a result of our lack of knowledge. Aleatory uncertainties, which are the ones we consider in this paper, are a result of their natural inherent variability, such as the wind speed. Because aleatory uncertainties are variable, they are analyzed with probabilistic methods and described by probability distributions.

A common way to study the effect of a probabilistic input on the output of a model is by Monte Carlo simulations (MC) or similar sampling methods, but one of their drawbacks is that many simulations of the model are needed to obtain accurate statistics of the outputs. Another approach is to use a stochastic expansion method, such as polynomial chaos (PC). In polynomial chaos, to approximate the statistics of the outputs a polynomial function is constructed that maps the uncertain inputs to the outputs of interest.

In this work, we use polynomial chaos, as opposed to Monte Carlo, because the functional relationship provided by polynomial chaos can be used to combine different levels of simulation fidelity (see section 6.4.3) and accurate statistics on the output can be obtained in many fewer simulations using polynomial chaos for problems with few uncertain variables, which is the case in this study.

6.4.1 Description of the 1D polynomial chaos method

Polynomial chaos is a method of propagating the uncertainties in a model's inputs to the model's outputs, by constructing a polynomial approximation to the model's response to stochastic input parameters ξ,

$$R(\xi) \approx \hat{R}(\xi) = \sum_{i=0}^{P} \alpha_i \phi_i(\xi), \tag{22}$$

where the larger the polynomial order P the closer the approximation $\hat{R}(\xi)$ is to the true response $R(\xi)$. The basis functions $\phi_i(\xi)$ are known orthogonal polynomials and the coefficients α_i are what need to be estimated in the polynomial chaos method. One approach to calculate the PC coefficients α_i is the spectral projection method which takes advantage of the orthogonality of the basis polynomials. In the spectral projection

Uncertain parameter	Probability distribution	Polynomial basis
x_0	Uniform	Legendre
L_g	Normal	Hermite
u_e	Gumbel	Numerically generated

Table 7: The polynomial basis used in the polynomial chaos method for each uncertain parameter.

method the first step to calculate the chaos coefficients is to multiply the PC expansion eq. (22) by $\phi_j(\xi)$ and $\rho(\xi)$, the density of the stochastic parameter, and then integrate over the probability space Ω,

$$\int_\Omega R(\xi)\phi_j(\xi)\rho(\xi)d\xi = \int_\Omega \sum_{i=0}^{\infty} \alpha_i \phi_i(\xi)\phi_j(\xi)\rho(\xi)d\xi. \tag{23}$$

Using the orthogonality of the basis polynomials with respect to the uncertain variable density,

$$\int \phi_i(\xi)\phi_j(\xi)\rho(\xi)d\xi = \delta_{i,j}, \tag{24}$$

and solving for the coefficients from eq. (23), we obtain

$$\alpha_i = \frac{\int_\Omega R(\xi)\phi_i(\xi)\rho(\xi)d\xi}{\int_\Omega \phi_i^2(\xi)\rho(\xi)d\xi} = \frac{\langle R(\xi), \phi_i(\xi)\rangle}{\langle \phi_i^2(\xi)\rangle} = \frac{1}{\langle \phi_i^2(\xi)\rangle}\int_\Omega R(\xi)\phi_i(\xi)\rho(\xi)d\xi. \tag{25}$$

A couple notes to keep in mind when evaluating the polynomial chaos coefficients equation eq. (25):

- The polynomial basis $\phi_i(\xi)$ is chosen such that it is orthogonal to the probability density function of the stochastic parameters $\rho(\xi)$ up to a constant. The common probability distributions have known basis polynomials[45], For stochastic parameters that do not follow one of the common probability distributions, a numerically generated polynomial basis can be constructed [44, 13]. The polynomial basis for the uncertain parameters considered in this paper are listed in table 7.
- The majority of the effort in solving for the coefficients resides in evaluating the integral, $\int_\Omega R(\xi)\phi_i(\xi)\rho(\xi)d\xi$, especially when $R(\xi)$ is expensive to evaluate, as the inner product $\langle \phi_i^2(\xi)\rangle$ for a particular polynomial basis is known. A common approach to evaluate the integral is by numerical quadrature

  $$\sum_{j=0}^{N} \omega_j R(\xi_j)\phi_i(\xi_j)\rho(\xi_j), \tag{26}$$

  where the weights ω_j and quadrature points ξ_j depend on the quadrature method used.

Once the coefficients α_i are known on top of having a functional relationship between the uncertain inputs and outputs

$$\hat{R}(\xi) = \sum_{i=0}^{P} \alpha_i \phi_i(\xi), \tag{27}$$

estimates of the statistics for the mean and variance can be computed from

$$\mu_R = \alpha_0, \tag{28}$$

$$\sigma_R^2 = \sum_{i=1}^{P} \alpha_i^2 \langle \phi_i^2(\xi)\rangle. \tag{29}$$

6.4.2 Multi-dimensional polynomial chaos and sparse grid construction

For multiple uncertain variables $\boldsymbol{\xi} = (\xi_1, \xi_2, \ldots \xi_d)$ the polynomial chaos expansion eq. (22) is written as

$$R(\boldsymbol{\xi}) \approx \hat{R}(\boldsymbol{\xi}) = \sum_{\mathbf{i} \in \mathcal{I}_p} \alpha_{\mathbf{i}} \boldsymbol{\Phi}_{\mathbf{i}}(\boldsymbol{\xi}), \tag{30}$$

where $\mathbf{i} = (i_1, i_2, \ldots, i_d)$ is a multi-index and the values of the elements $i_j \in \mathbb{N}$ depend on how the expansion is truncated, i.e., on how the index set $\mathcal{I}_p$ is defined. There are two common ways in which to define the index set: "total-order expansion" and "tensor-product expansion". In "total-order expansion" a total polynomial order bound p is enforced

$$\mathcal{I}_p = \{\mathbf{i} : |\mathbf{i}| \leq p\}, \quad |\mathbf{i}| = i_1 + i_2 + \cdots + i_d. \tag{31}$$

Whereas in "tensor-product expansion" a per-dimension polynomial order bound p_j is enforced

$$\mathcal{I}_p = \{\mathbf{i} : i_j \leq p_j, \ j = 1, \ldots, d\}. \tag{32}$$

The basis functions $\boldsymbol{\Phi}_{\mathbf{i}}(\boldsymbol{\xi})$ are given by products of one-dimensional orthogonal polynomials ϕ_{i_j},

$$\boldsymbol{\Phi}_{\mathbf{i}}(\boldsymbol{\xi}) = \prod_{j=1}^{d} \phi_{i_j}(\xi_j). \tag{33}$$

Similarly to the 1D case, the coefficients of the expansion are calculated from

$$\alpha_{\mathbf{i}} = \frac{1}{\langle \boldsymbol{\Phi}_{\mathbf{i}}^2(\boldsymbol{\xi}) \rangle} \int_{\Omega} R(\boldsymbol{\xi}) \boldsymbol{\Phi}_{\mathbf{i}}(\boldsymbol{\xi}) \rho(\boldsymbol{\xi}) \mathrm{d}\boldsymbol{\xi}, \tag{34}$$

where $\rho(\boldsymbol{\xi}) = \prod_{j=1}^{d} \rho_j(\xi_j)$ is the joint probability density of the stochastic parameters over the support $\Omega = \Omega_1 \times \cdots \times \Omega_d$. Same as in the 1D case the majority of the effort in computing the coefficients resides in evaluating the integral $\int_{\Omega} R(\boldsymbol{\xi}) \boldsymbol{\Phi}_{\mathbf{i}}(\boldsymbol{\xi}) \rho(\boldsymbol{\xi}) \mathrm{d}\boldsymbol{\xi}$. To evaluate the integral tensor product quadrature $\mathcal{Q}_{\mathbf{i}}$ can be used, but the number of quadrature points in tensor product quadrature grows exponentially with the number of dimensions d. To alleviate the exponential growth in quadrature points sparse grid quadrature can be used. Sparse grid quadrature is constructed from a linear combination of tensor product quadrature grids $\mathcal{Q}_{\mathbf{i}}$ in such a way that high accuracy is preserved while using only a relative small number of grid(quadrature) points.[24, 12, 8] The isotropic sparse grid level q ($q \in \mathbb{N}$) used to perform the integration in eq. (34) is defined as

$$\mathcal{A}_{q,d}(R) = \sum_{q-d+1 \leq |\mathbf{i}| \leq q} (-1)^{q-|\mathbf{i}|} \binom{d-1}{q-|\mathbf{i}|} \mathcal{Q}_{\mathbf{i}}(R) \tag{35}$$

where as q increases more quadrature points are used and the integral is evaluated more accurately. The number of quadrature points depends on the number of uncertain variables and on the distributions of the uncertain variables. Table 8 lists the number of quadrature points used for our particular problem where we have $d = 3$ uncertain variables which follow the distributions in table 7.

6.4.3 Multi-fidelity uncertainty quantification with polynomial chaos

The goal of the multi-fidelity uncertainty quantification is to accurately characterize the high-fidelity system response $R_{high}(\boldsymbol{\xi})$ with less computational effort by using information obtained from the low-fidelity system response $R_{low}(\boldsymbol{\xi})$ as opposed to solely using the high-fidelity response. There are different methods of incorporating the information from the low-fidelity response.[24] Here we will do so by means of an additive correction function,

$$R_{corr}(\boldsymbol{\xi}) = R_{high}(\boldsymbol{\xi}) - R_{low}(\boldsymbol{\xi}). \tag{36}$$

In multi-fidelity UQ instead of approximating the high-fidelity function directly via polynomial chaos

$$R_{high}(\boldsymbol{\xi}) \approx \hat{R}_{high}(\boldsymbol{\xi}) = \sum_{\mathbf{i} \in \mathcal{I}_p} \alpha_{\mathbf{i}} \boldsymbol{\Phi}_{\mathbf{i}}(\boldsymbol{\xi}), \tag{37}$$

Sparse grid level	Number of evaluations
1	9
2	44
3	158
4	455
5	1099

Table 8: Number of function evaluations (quadrature points) in each sparse grid level. The higher levels reuse the evaluations in the lower levels.

we approximate it from the polynomial chaos expansions of the low-fidelity and correction function

$$R_{high}(\boldsymbol{\xi}) \approx \tilde{R}_{high}(\boldsymbol{\xi}) = \hat{R}_{low}(\boldsymbol{\xi}) + \hat{R}_{corr}(\boldsymbol{\xi}). \tag{38}$$

The multi-fidelity approach could be beneficial if an accurate expansion of the correction function $\hat{R}_{corr}$ can be obtained with less computational effort, i.e., with less simulations(quadrature points) than the high-fidelity function $\hat{R}_{high}$ and if the low-fidelity model is a good approximation to the high-fidelity model[24]. A priori, it is hard to know for a particular problem if the conditions on the low-fidelity and correction function would be satisfied and even then if the multi-fidelity approach will lead to any computational savings. But for some problems large (80%) computational savings can be obtained.[24]

6.5 Results

First we show results for a particular gust realization and then we follow with the results from the uncertainty quantification study.

A simulation in SU^2 of the gust convecting passed the turbine blades is shown in fig. 15. To help visualization a circle is drawn around the blade we will refer to as "*Blade*-1". The position of *Blade*-1 in figs 15(a) and 14(b) is the 0° position. *Blade*-1 advances by 90° in each frame and each row of fig. 15 represents a full revolution of the turbine.

As the gust convects pass the blades it changes the blades angles of attack. The angle of attack that a blade sees during a revolution for normal operating conditions (no-gust) is shown in fig. 16. If the gust interacts with the blade when it is already at a high angle of attack it can cause the flow to separate and the blade to stall. An angle of attack sweep for the blade (SNL 0018/50 airfoil) showed that the blade stalls at around 12° for both Euler and RANS simulations in SU^2. Also, the Euler and RANS simulations agreed well for the angle of attack sweep given us confidence that the results obtained by the Euler simulations are reasonable even if gust caused the blade to stall.

The most interaction *Blade*-1 has with the gust is during the second revolution of the turbine (figs. 15(e), 15(f), 15(g) and 15(h)). The normal and tangential forces on *Blade*-1 during the second revolution are shown in figs. 17 and 18, respectively. For comparison purposes (figs. 17 and 18) include the forces obtained from the low-fidelity model and for the normal operating conditions when there is no gust. The low-fidelity model under predicts the maximum forces when there is no gust and more noticeably when there is a gust. The gust has a bigger effect on the high-fidelity simulation because on top of changing the angle of attack the gust can cause unsteady aerodynamic effects which are not captured by the low-fidelity model. For instance the gust can cause the blade to stall, followed by a vortex convecting over the blade which can cause large variations in the forces and the larger discrepancies between the high and low-fidelity model.

For the uncertainty quantification study, we picked the maximum normal $C_{n,max}$ and maximum tangential force $C_{t,max}$ as our quantities of interest (QOI). We picked these QOI because as seen in figs. 17 and 18 they are affected by the uncertain gust and if they are large enough they can cause turbine failure. The gust interaction in figs. 17 and 18 is a very benign interaction as the effect on the maximum forces is small. This particular gust realization is from setting the gust parameters to their mean values.

The maximum number of gust realizations used for the high-fidelity case is 455 (sparse grid level 4) and for the low-fidelity case is 1099 (sparse grid level 5). A high-fidelity simulation takes about 30 minutes on 36 processors and a low-fidelity simulation 1 minute on 1 processor. The difference in simulation time between

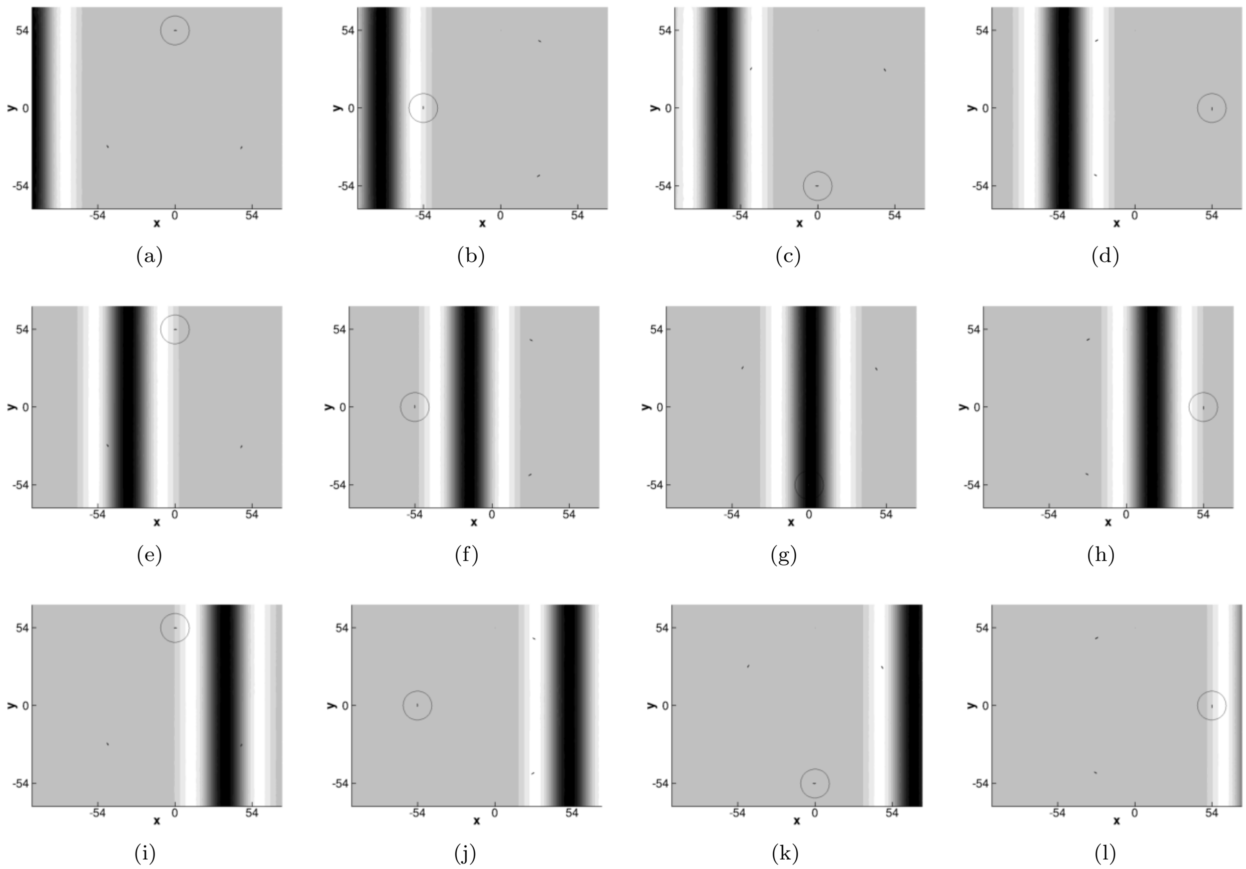

Figure 15: Evolution of the gust. A circle is drawn around *Blade*-1 to help with visualization. In each frame *Blade*-1 advances by 90° and each row represents a full revolution of the blade. The gust interactions lasts from 3 to 4 revolutions depending on the uncertain gust realization. The figure shows the gust velocity as compared to the free-stream velocity and the darker the color the higher the gust value.

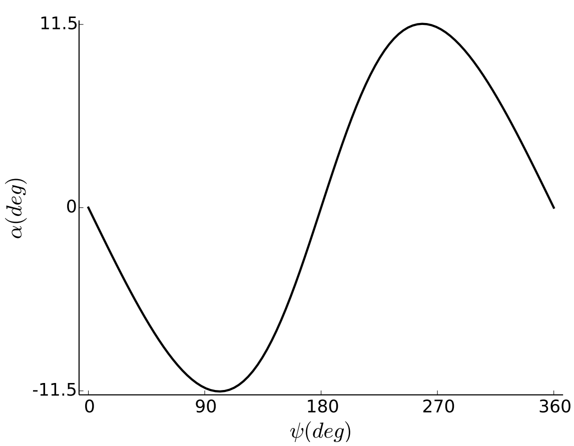

Figure 16: Angle of attack seen by the blades in normal operating conditions.

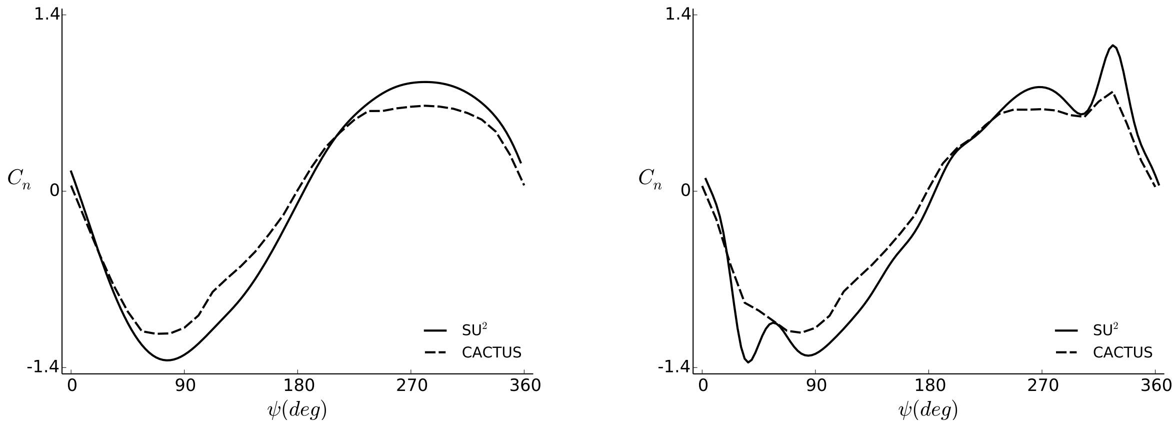

(a) No Gust (b) Gust

Figure 17: Comparison of the normal force coefficient C_n as a function of azimuth ψ between the high-fidelity tool SU^2 and the low-fidelity tool CACTUS. For the normal operating conditions CACTUS compares well with SU^2 (a), but CACTUS fails to capture all the variability introduced by the gust (b), which is expected of the low-fidelity tool.

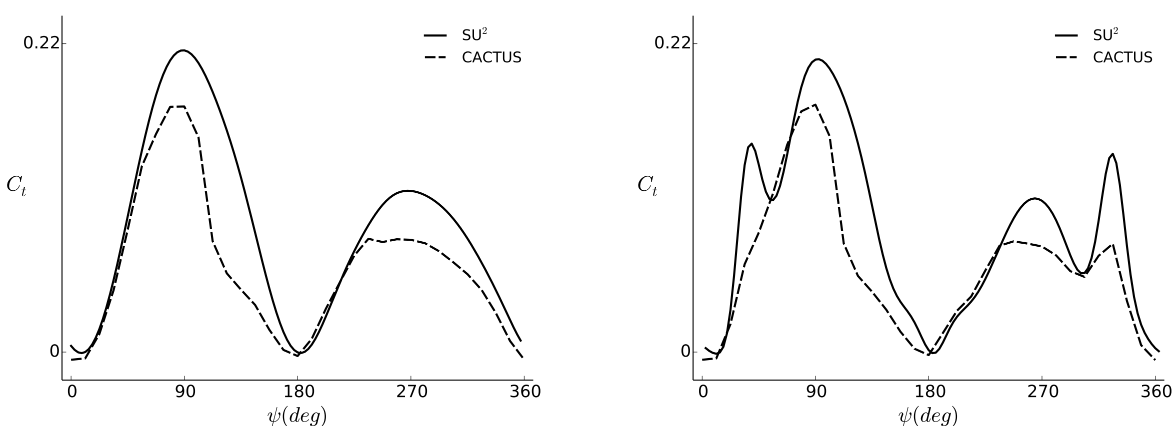

(a) No Gust (b) Gust

Figure 18: Comparison of the tangential force coefficient C_t as a function of azimuth ψ between the high-fidelity tool SU^2 and the low-fidelity tool CACTUS. For the normal operating conditions CACTUS compares well with SU^2 (a), but CACTUS fails to capture all the variability introduced by the gust (b), which is expected of the low-fidelity tool.

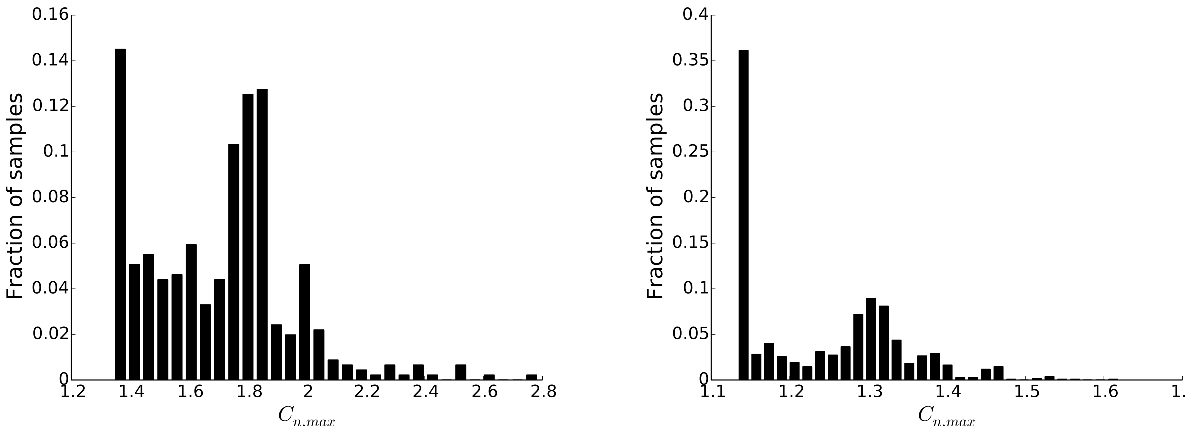

(a) High-fidelity - $C_{n,max}$

(b) Low-fidelity - $C_{n,max}$

Figure 19: Histogram of the maximum normal force for the high-fidelity (455 samples) and low-fidelity (1099 samples).

the high and low-fidelity is 3 orders of magnitude. Table 8 lists the number of samples in each sparse grid level. The higher sparse grid levels reuse the simulations from the lower sparse grid levels. A histogram of the output for the maximum normal force for the low and high-fidelity tool is shown in fig. 19 and for the maximum tangential force in fig. 20. There are many cases for which the gust does not affect the maximum forces, this is especially the case for the low-fidelity tool for which about 40% of its samples have their normal operating condition maximum. The spread in the high-fidelity is more pronounced and the maximum force can reach very large values as compared to the low-fidelity results.

The sparse grid level 4 samples are shown in fig. 21. These samples are colored based on the maximum normal force. The samples values are symmetrically distributed for the gust starting position x_0 and the gust length L_g which follow symmetric distributions (see table 5) and for the gust amplitude u_e the samples are more heavily concentrated on values higher than its mean. The highest values of the maximum force occur at the highest values of the gust amplitude. A plot for the maximum tangential force shows a similar behavior.

In fig. 21 there is the least amount of variation along the gust length L_g axis. Holding L_g fixed at its mean value, fig. 22 shows the samples for sparse level 1,2,3 and 4. These samples are again colored based on the maximum normal force. We see that as the sparse grid level is increased there are samples with larger gust amplitude values which cause larger values for the maximum normal force. These large values can slow down the convergence of the statistics for the maximum forces.

Also holding the gust amplitude fixed we can visualize how $C_{n,max}$ changes as a function of the gust starting position for the high and low-fidelity tool and also visualize what the correction function (difference between the high and low-fidelity) might look like for performing the multi-fidelity uncertainty quantification (fig. 23). For this slice of the data, the complexity of the correction function is similar to the high-fidelity and the low-fidelity does not fully follow the the high-fidelity trend, which are not ideal conditions to see very large computational savings when using multi-fidelity UQ.

The relative change in the mean and variance of the maximum forces between consecutive sparse grid levels is shown in figs. 24 and 25, for both the multi-fidelity and high-fidelity. In the multi-fidelity case the starting sparse grid level corresponds to the level used to approximate the correction function and the multi-fidelity uses a sparse grid level 5 for the low-fidelity.

The decrease in the relative change of the variance between succesive sparse grid levels (1-2, 2-3, 3-4) shows that the statistics are converging. Also, the value of the relative change in the mean for both forces converges rapidly to around 1%. The relative change in the variance and the mean is with respect to the variance and mean obtained from the sparse grid level 4 samples. For the statistics of $C_{n,max}$ and $C_{t,max}$ shown in figs. 24 and 25 the multi-fidelity approach provides more accurate statistics for most of the cases with lower number of samples.

More accurate statistics for a lower number of samples (lower computational cost) is also observed for two

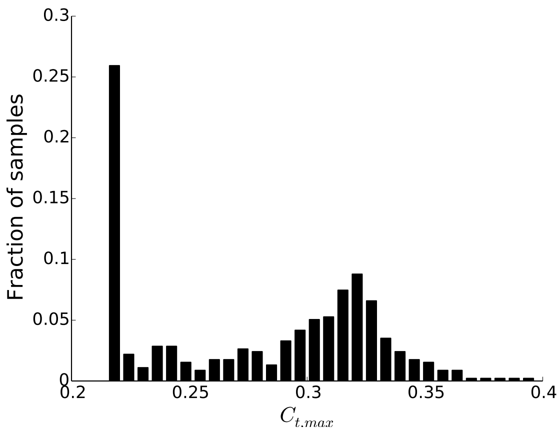

(a) High-fidelity - $C_{t,max}$

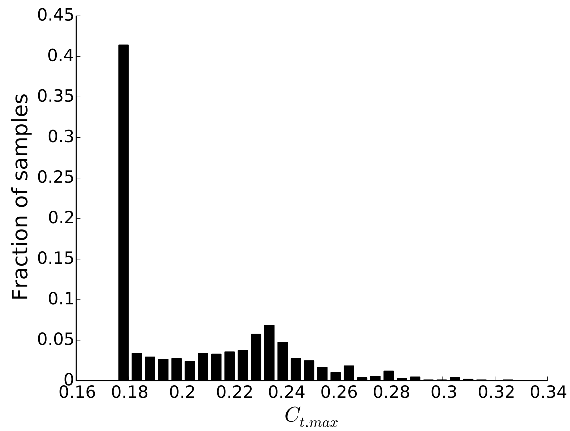

(b) Low-fidelity - $C_{t,max}$

Figure 20: Histogram of the maximum tangential force for the high-fidelity (455 samples) and low-fidelity (1099 samples).

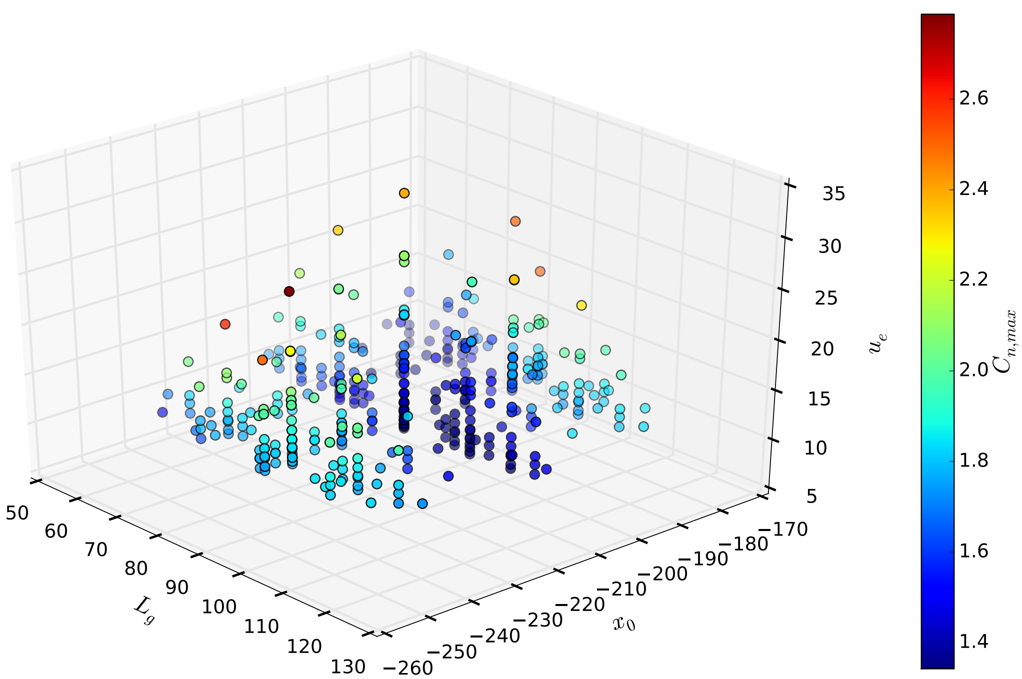

Figure 21: Sparse grid level 4 samples colored by the maximum normal force obtained by using the high-fidelity tool (SU^2).

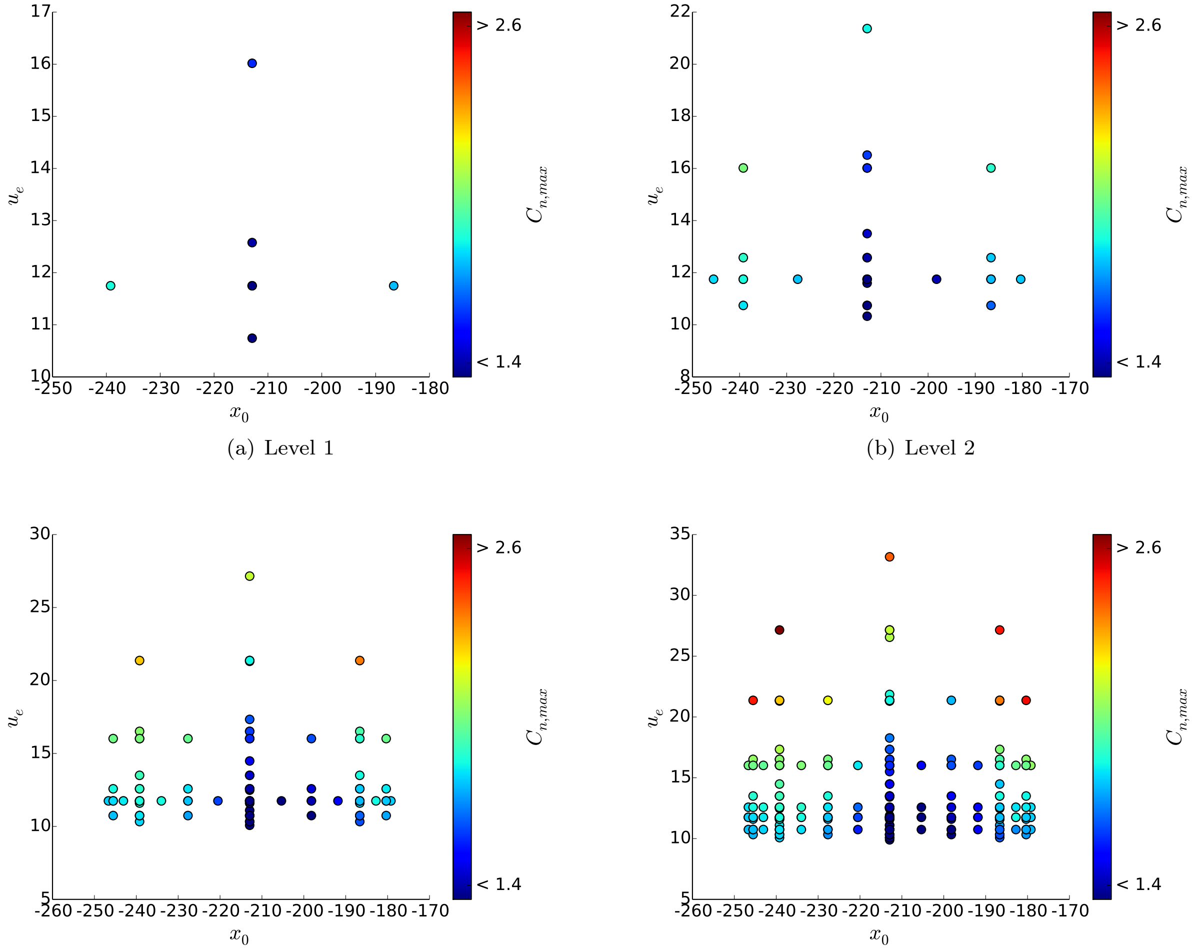

(a) Level 1 (b) Level 2

(c) Level 3 (d) Level 4

Figure 22: Maximum force response to the uncertain variables x_0 and u_e. The gust length L_g is hold constant at its mean value.

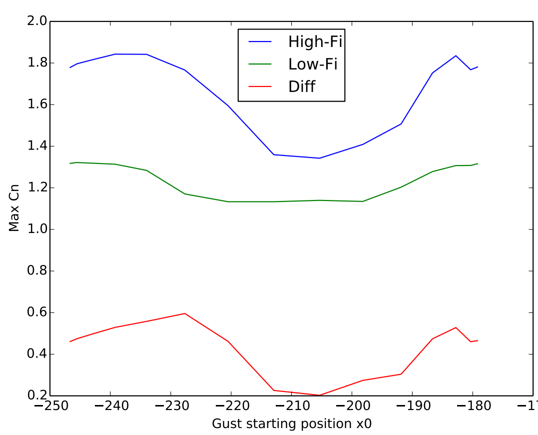

Figure 23: Maximum force response as a function of gust starting position. The difference function is of similar complexity than the high-fidelity function.

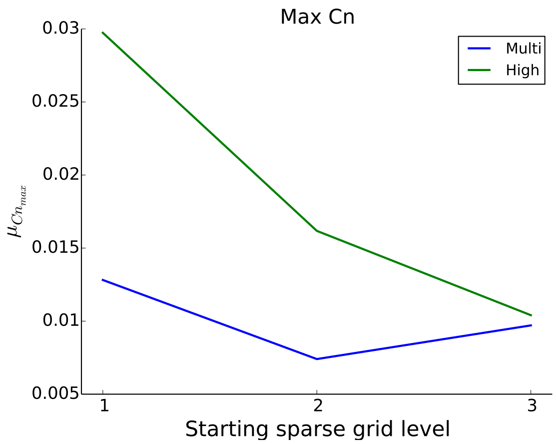

(a) Mean

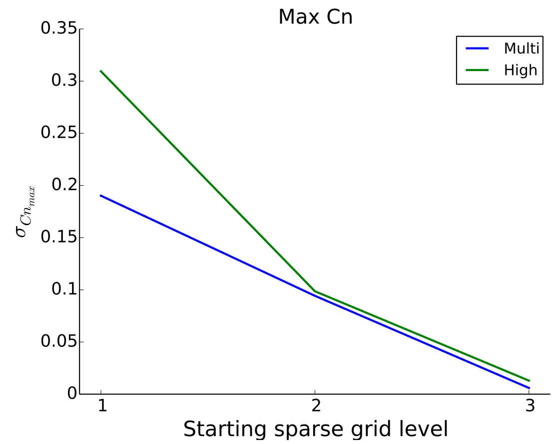

(b) Variance

Figure 24: Convergence of maximum normal force statistics.

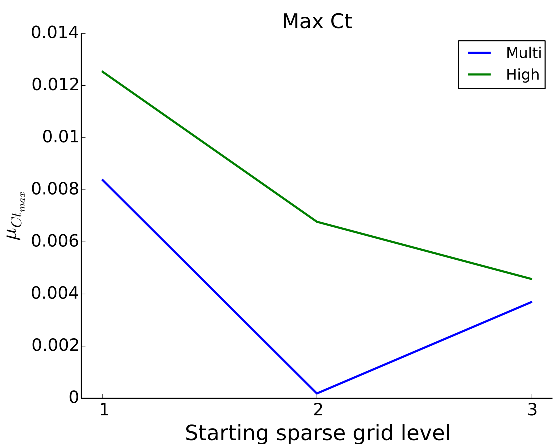

(a) Mean

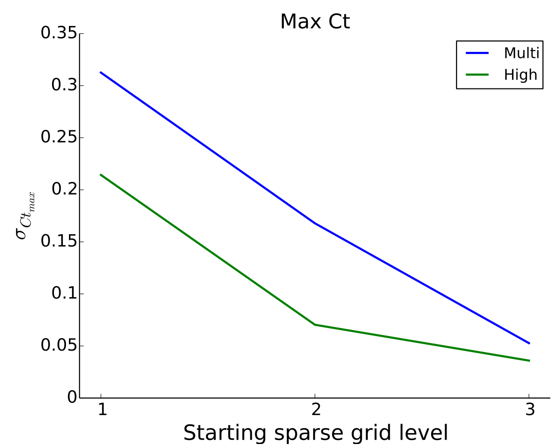

(b) Variance

Figure 25: Convergence of the maximum tangential force statistics.

other quantities of interest, the total variation in the normal and tangential force caused by the gust (figs. 26 and 27). The total variation,

$$TV\text{-}Cn = \frac{|Cn_{gust} - Cn_{nogust}|_1}{|Cn_{nogust}|_1}, \tag{39}$$

is an integrated measure of the effect of the gust as opposed to the maximum values which are point values.

6.6 Conclusions

In this portion of the work in this grant, we have explored the influence of a uncertain extreme gust on the maximum normal and maximum tangential force on the blades of a VAWT. The extreme gust is defined by three uncertain variables, the gust starting position x_0, the gust length L_g, and the gust amplitude u_e. The maximum forces are most susceptible to the gust amplitude and the gust starting position. We studied the effect of the gust with a low-fidelity tool CACTUS (blade element/vortex lattice aerodynamic solver) and a high-fidelity tool SU^2 (CFD solver). To study the effect of a gust in the CFD solver, we developed a practical method that allows us to simulate a gust that changes its magnitude in the flow direction (non-divergent free gust) by combining the field velocity method (FVM) and the geometric conservation law (GCL).

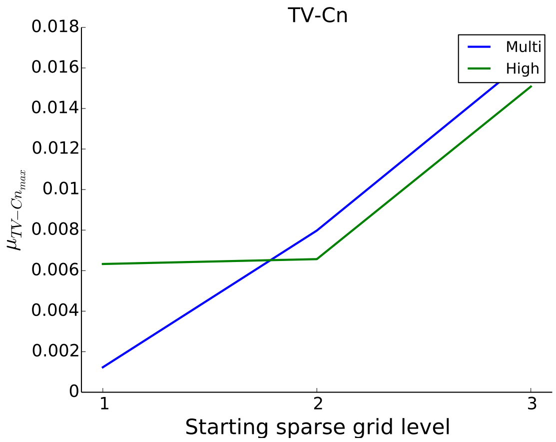

(a) Mean

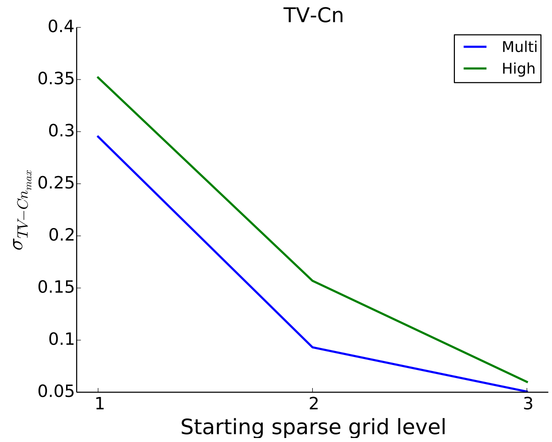

(b) Variance

Figure 26: Convergence of the total variation normal force statistics.

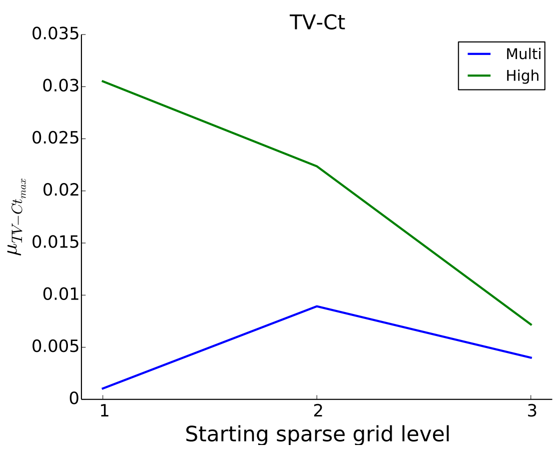

(a) Mean

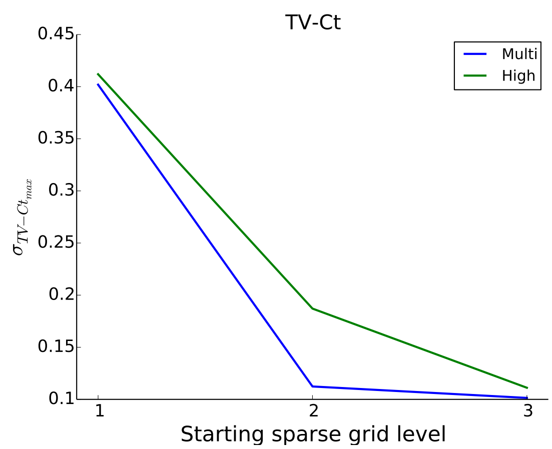

(b) Variance

Figure 27: Convergence of the total variation tangential force statistics.

We found that the proposed multi-fidelity uncertainty quantification methodology provides better estimates of the statistics of interest for a lower number of high-fidelity simulations. The multi-fidelity methodology uses polynomial chaos to create an approximation to the high-fidelity statistics via a correction function based on the difference between the high and low-fidelity simulations. Simulating the gust with the low-fidelity tool underestimates the value of the mean and the variance for the maximum forces on the blade when compared to the high-fidelity tool ("true solution"). Also, simulating the gust at its deterministic "most likely" realization under predicts the maximum forces on the blade when compared to the mean values calculated by the uncertainty quantification study. A good estimate of the high-fidelity mean for the maximum forces is obtained in only a few (9 - sparse grid level 1) high-fidelity simulations.

7 Closing Remarks

7.1 Observations on methods

- This project is developing a broad suite of scalable and robust UQ methods, covering adaptive p- and h-refinement with adjoint-enhancement over structured and unstructured grids.
- We are now starting to build on top of this core UQ machinery with investments in error balancing and multifidelity modeling.

7.2 Observations on applications

- We have demonstrated the deployment of state of the art UQ methodologies to current production simulation tools for wind turbine performance.
- These low fidelity simulation tools have exhibited nonsmooth behavior, particularly when modeling turbulent in-flows, motivating an increased emphasis on algorithmic robustness.

7.3 Impact

Key programmatic impacts of this effort include:

- NREL is currently developing their next-generation modeling and simulation framework and they are closely following the developments in this project. Based on recommendations from our team, NREL is developing their framework using OpenMDAO and DAKOTA as key foundational components.
- Discussions with senior leadership in NREL have been used to highlight the importance of UQ techniques (at many levels) in the development of the next generation of their predictive tool capability. Senior leadership has expressed interest in pursuing such techniques as a high-priority item as soon as their basic framework has been established.
- Progress has been made in deploying the DAKOTA framework to Sandia-led research supported by EERE's Wind Power Program [2].

References

[1] *IEC 61400-1 : Wind turbines - Part 1: Design requirements*, tech. rep., International Electrotechnical Commission, 2005.

[2] M. Barone, J. Paquette, B. Resor, and L. Manuel, *Decades of wind turbine load simulation*, in Proceedings of the 51st AIAA Aerospace Sciences Meeting, Grapevine, TX, January 7–10 2012.

[3] R. Bartels, *Development, Verification and Use of Gust Modeling in the NASA Computational Fluid Dynamics Code FUN3D*, no. October, 2012.

[4] J. T. BATINA, *Unsteady Euler airfoil solutions using unstructured dynamic meshes*, AIAA Journal, 28 (1990), pp. 1381–1388.

[5] S. P. Domino, *Towards verification of sliding mesh algorithms for complex applications using mms*, in Proceedings of 2010 Center for Turbulence Research Summer Program, Stanford University, CA, June 27-July 23. 2010.

[6] D. L. Donoho, A. Maleki, and A. Montanari, *Message-passing algorithms for compressed sensing*, Proceedings of the National Academy of Sciences, 106 (2009), pp. 18914–18919.

[7] K. Duraisamy, J. J. Alonso, F. Palacios, and P. Chandrasekhar, *Adjoint based error estimation for high speed flow computations*, in Proceedings of the 48th AIAA Aerospace Sciences Meeting, Orlando, FL, January 2010.

[8] M. S. Eldred, *Design Under Uncertainty Employing Stochastic Expansion Methods*, International Journal for Uncertainty Quantification, 1 (2011), pp. 119–146.

[9] M. S. Eldred, E. T. Phipps, and K. R. Dalbey, *Adjoint enhancement within global stochastic methods*, in Proceedings of the SIAM Conference on Uncertainty Quantification, Raleigh, NC, April 2–5 2012.

[10] M. S. Eldred and L. P. Swiler, *Towards goal-oriented stochastic design employing adaptive collocation methods*, in Proceedings of the 13th AIAA/ISSMO Multidisciplinary Analysis and Optimization Conference, Fort Worth, TX, Sept. 13-15 2010.

[11] C. Farhat, P. Geuzaine, and C. Grandmont, *The Discrete Geometric Conservation Law and the Nonlinear Stability of ALE Schemes for the Solution of Flow Problems on Moving Grids*, Journal of Computational Physics, 174 (2001), pp. 669–694.

[12] T. Gerstner and M. Griebel, *Numerical integration using sparse grids*, Numerical algorithms, 18 (1998), pp. 209–232.

[13] G. Golub and J. Welsch, *Calculation Of Gauss Quadrature Rules*, Mathematics of Computation, (1969).

[14] A. Gopinath and A. Jameson, *Time spectral method for periodic unsteady computations over two- and three-dimensional bodies*, in Proceedings of the 43rd AIAA Aerospace Sciences Meeting, Reno, NV, January 2005.

[15] M. Islam, D. S.-K. Ting, and A. Fartaj, *Aerodynamic models for Darrieus-type straight-bladed vertical axis wind turbines*, Renewable and Sustainable Energy Reviews, 12 (2008), pp. 1087–1109.

[16] J. D. Jakeman and S. G. Roberts, *Local and dimension adaptive stochastic collocation for uncertainty quantification*, in Proceedings of the Workshop on Sparse Grids and Applications, Bonn, Germany, May 16–20 2011.

[17] A. Jameson, *Time dependent calculations using multigrid, with applications to unsteady flows past airfoils and wings*, AIAA, 1991.

[18] A. Jameson, W. Schmidt, and E. Turkel, *Numerical solutions of the Euler equations by finite volume methods using Runge-Kutta time-stepping schemes*, AIAA paper, M (1981), pp. 1–19.

[19] a. Korobenko, M.-C. Hsu, I. Akkerman, and Y. Bazilevs, *Aerodynamic Simulation of Vertical-Axis Wind Turbines*, Journal of Applied Mechanics, 81 (2013), p. 021011.

[20] G. C. Larsen and K. S. Hansen, *Rational calibration of four IEC 61400-1 extreme external conditions*, Wind Energy, 11 (2008), pp. 685–702.

[21] M. Lesoinne and C. Farhat, *Geometric conservation laws for flow problems with moving boundaries and deformable meshes, and their impact on aeroelastic computations*, Computer methods in applied mechanics and ..., 7825 (1996).

[22] C. Li, S. Zhu, Y.-l. Xu, and Y. Xiao, *2.5D large eddy simulation of vertical axis wind turbine in consideration of high angle of attack flow*, Renewable Energy, 51 (2013), pp. 317–330.

[23] J. Murray and M. Barone, *The Development of CACTUS, a Wind and Marine Turbine Performance Simulation Code*, in 49th AIAA Aerospace Sciences Meeting, no. January, Reston, Virigina, Jan. 2011, American Institute of Aeronautics and Astronautics, pp. 1–21.

[24] L. W.-T. Ng and M. Eldred, *Multifidelity Uncertainty Quantification Using Non-Intrusive Polynomial Chaos and Stochastic Collocation*, in 53rd AIAA/ASME/ASCE/AHS/ASC Structures, Structural Dynamics and Materials Conference 20th AIAA/ASME/AHS Adaptive Structures Conference 14th AIAA, no. April, Reston, Virigina, Apr. 2012, American Institute of Aeronautics and Astronautics, pp. 1–17.

[25] L. W. T. Ng and M. S. Eldred, *Multifidelity uncertainty quantification with non-intrusive polynomial chaos and stochastic collocation*, in Proceedings of the 14th AIAA Non-Deterministic Approaches Conference, Honolulu, HI, April 23–26 2012.

[26] J. Oler, J. Strickland, B. Im, and G. Graham, *Dynamic stall regulation of the darrieus turbine*, in SANDIA REPORT, SAND83-7029 UC-261, August 1983.

[27] F. Palacios, J. Alonso, K. Duraisamy, M. Colonno, J. Hicken, A. Aranake, A. Campos, S. Copeland, T. Economon, A. Lonkar, T. Lukaczyk, and T. Taylor, *Stanford University Unstructured (SU2): An open-source integrated computational environment for multi-physics simulation and design*, in 51st AIAA Aerospace Sciences Meeting, no. January, Reston, Virigina, Jan. 2013, American Institute of Aeronautics and Astronautics, pp. 1–60.

[28] F. Palacios, K. Duraisamy, A. Aranake, S. R. Copeland, T. D. Economon, A. K. Lonkar, T. W. Lukaczyk, K. R. Naik, S. Padron, and J. J. Alonso, *Stanford University Unstructured (SU2): Analysis and Design Technology for Turbulent Flows*, in 52nd Aerospace Sciences Meeting, no. January, Reston, Virginia, Jan. 2014, American Institute of Aeronautics and Astronautics, pp. 1–33.

[29] V. Parameswaran and J. D. Baeder, *Indicial Aerodynamics in Compressible Flow-Direct Computational Fluid Dynamic Calculations*, Journal of Aircraft, 34 (1997), pp. 131–133.

[30] d. N. C. Q. D. W. J. A.-C. J. I. G. Petrone, G., *Wind turbine optimization under uncertainty with high performance computing*, in Proceedings of the 29th AIAA Applied Aerodynamics Conference, Honolulu, HI, June 27–30 2011.

[31] G. Petrone, C. deNicola, J. Witteveen, and G. Iaccarino, *Wind turbine optimization under uncertainty with high performance computing*, in AIAA 2011 3806, 2011.

[32] D. E. Raveh, *CFD-Based Models of Aerodynamic Gust Response*, Journal of Aircraft, 44 (2007), pp. 888–897.

[33] F. Scheurich and R. Brown, *Modelling the aerodynamics of vertical axis wind turbines in unsteady wind conditions*, Wind Energy, (2012), pp. 91–107.

[34] F. Scheurich, T. Fletcher, and R. Brown, *Simulating the aerodynamic performance and wake dynamics of a vertical axis wind turbine*, Wind Energy, (2011).

[35] R. Singh and J. D. Baeder, *Direct Calculation of Three-Dimensional Indicial Lift Response Using Computational Fluid Dynamics*, Journal of Aircraft, 34 (1997), pp. 465–471.

[36] J. H. Strickland, T. Smith, and K. Sun, *A vortex model of the darrieus turbine: An analytical and experimental study*, in SAND81-7017, Sandia National Laboratories, NM, 1981.

[37] S. Takahashi, J. Hamada, and Y. Takashi, *Numerical and experimental studies of airfoils suitable for Vertical Axis Wind Turbines and an application of wind-energy collecting structure for higher performance*, Journal of Wind Engineering, (2006), pp. 327–330.

[38] I. G. E. M. S. Tang, G., *Global sensitivity analysis for stochastic collocation expansion*, in Proceedings of the 51st AIAA/ASME/ASCE Structures, Structural Dynamics, and Materials Conference, Orlando, FL, April 12–15 2010.

[39] J. Tangler and D. Kocurek, *Wind Turbine Post-Stall Airfoil Performance Characteristics Guidelines for Blade-Element Momentum Methods*, in 43rd AIAA Aerospace Sciences Meeting and Exhibit, Reston, Virigina, Jan. 2005, American Institute of Aeronautics and Astronautics, pp. 1–10.

[40] D. Veldkamp, *Chances in Wind Energy: A Probabilistic Approach to Wind Turbine Fatigue Design*, PhD thesis, Tecnical University of Delft, 2006.

[41] C. Wales, D. Jones, and A. Gaitonde, *Reduced order modelling for aeroelastic aerofoil response to a gust*, in 51st AIAA Aerospace Sciences Meeting, no. January, Grapevine, Texas, 2013, American Institute of Aeronautics and Astronautics, pp. 1–16.

[42] K. Walter, C. C. Weiss, A. H. P. Swift, C. J., and K. N. D., *Speed and direction shear in the stable nocturnal boundary layer*, J. Solar Energy Engineering, 131 (2009).

[43] J. Witteveen and G. Iaccarino, *Simplex stochastic collocation with random sampling and extrapolation for non-hypercube probability spaces*, SIAM Journal of Scientific Computing, accepted (2011).

[44] J. A. Witteveen and H. Bijl, *Modeling Arbitrary Uncertainties Using Gram-Schmidt Polynomial Chaos*, in 44th AIAA Aerospace Sciences Meeting and Exhibit, no. January, Reston, Virigina, Jan. 2006, American Institute of Aeronautics and Astronautics.

[45] D. Xiu and G. Karniadakis, *The Wiener–Askey polynomial chaos for stochastic differential equations*, SIAM Journal on Scientific Computing, 02912 (2002), pp. 1–26.

[46] A. Zaide and D. Raveh, *Numerical Simulation and Reduced-Order Modeling of Airfoil Gust Response*, in 17th AIAA Computational Fluid Dynamics Conference, no. June, Reston, Virigina, June 2005, American Institute of Aeronautics and Astronautics, pp. 1–16.

[47] Babuska, I., and Miller, A., "The Post Processing approach in the Finite Element Method, Part 1: Calculation of Stresses, Displacements and Other High Order Derivatives of Displacements," *International Journal of Numerical Methods in Engineering,* Vol. 26, pp. 1085–1109, 1984.

[48] Baker, T., "Mesh Adaptation Strategies for Problems in Fluid Dynamics," Finite Elements in Analysis and Design, 25 pp. 243–273, 1997.

[49] Giles, M., Larson, M., Levenstam, J., and Suli, E., "Adaptive Error Control for Finite Element Approximations of the Lift and Drag Coefficients in Viscous flow," Report NA-97/06, Oxford University Computing Laboratory, 1997.

[50] Pierce, N., and Giles, M., "Adjoint and Defect Error Bounding and Correction for Functional Estimates," *Journal of Computational Physics,* Vol. 200, pp. 769–794, 2002.

[51] Venditti, D., and Darmofal, D., "Anisotropic Grid Adaptation for Functional Outputs: Application to Two-dimensional Viscous Flows," *Journal of Computational Physics,* Vol. 187, pp. 22–46, 2002.

[52] Gopinath, A., and Jameson, A., "Time spectral method for periodic unsteady computations over two- and three- dimensional bodies," AIAA Paper 2005-1220, Reno, NV, January 2005.

[53] van der Weide, E., Gopinath, A., and Jameson, A., "Turbomachinery applications with the time spectral method," AIAA Paper 2005-4905, Toronto, Canada, June 2005.

[54] Duraisamy, K., Alonso, J. and Chandrashekar, P., "Goal-Oriented Uncertainty Propagation Using Stochastic Adjoints," AIAA Paper 2011-3412, Honolulu, Hawaii, June 2011.

[55] Roe, P., "Approximate Riemann Solvers, Parameter Vectors and Difference Schemes," *Journal of Computational Physics,* Vol. 135, (2), pp. 250–258, 1997

[56] Mader, C. A., "ADjoint: An Approach for the Rapid Development of Discrete Adjoint Solvers," Master's Thesis, University of Toronto, Toronto, Canada, 2007.

[57] Balay, S., Buschelman, K., Gropp, W. D., Kaushik, D., Knepley, M. G., McInnes, L. C., Smith, B. F., and Zhang, H., PETSc Web page, 2001. http://www.mcs.anl.gov/petsc.

[58] Najm, H. N., "Uncertainty Quantification and Polynomial Chaos Techniques in Computational Fluid Dynamics," *Annual Review of Fluid Mechanics* Vol. 41, pp. 35-52, 2009.

[59] Oler, J. W., Strickland, J. H., Im, B. J., and Graham, G. H., "Dynamic Stall Regulation of the Darrieus Turbine," Contractor Report, SAND83-7029, 1983.